Synthesis and Characterization of $BaFe_{12}O_{19}$ for EMI Shielding

By

Mirza Imran Aziz Baig

School of Chemical and Materials Engineering

National University of Sciences and Technology

2021

Synthesis and Characterization of $BaFe_{12}O_{19}$ for EMI Shielding

Name: Mirza Imran Aziz Baig

Reg. No: 00000205010

This thesis is submitted as a partial fulfillment of the requirements for the degree of

Master of Materials and Surface Engineering

Supervisor Name: Dr. -Ing. Farhan Javaid

School of Chemical and Materials Engineering (SCME)

National University of Sciences and Technology (NUST)

H-12 Islamabad, Pakistan

August, 2021

Dedication

I would like to dedicate this work to the Holy Prophet Muhammad (PBUH), to my wife, my son Muhammad Hassaan Mirza, to my little daughters Fatima and Amna. This work is a sign of my love to them especially to Holy Prophet Muhammad (PBUH).

Acknowledgements

''Praise is to the One, the Almighty, the merciful and the beneficent Allah, who is the source of all knowledge and wisdom, taught us what we knew not''.

I offer humblest thank to the Holy Prophet (PBUH), a model of knowledge and guidance and for humanity.

It is my privilege to express deepest appreciation and gratitude from the core of my heart to my research supervisor Dr. -Ing. Farhan Javaid and the Guidance Examination Committee (GEC) members, Dr. I. H. Gul and Dr. Muhammad Aftab Akram for their constant support, advice, valuable comments, and efficient supervision at every stage of research work especially in this pandemic situation. Without their support, this could not have been possible. I express my deep gratitude to Prof. Ir. Dr. Amir Azam Khan (Principal SCME) and Prof. Dr. Zakir Hussain (HoD ME) for their efforts to keep the environment congenial for research and study.

I am much thankful to Dr. Muhammad Mansoor from Institute of Industrial Control Systems (IICS), Rawalpindi for his support and guidance throughout my research work.

I am also grateful to my father Mr. Mirza Aziz Baig, my brothers and all my friends for giving me encouragement, appreciation and help in the completion of this project.

Sincerely,
Mirza Imran Aziz Baig

Abstract

In present work, the cobalt (Co) doped Barium hexaferrite ($Ba_{(1-x)}$ Fe_{12} $(Co)_xO_{19}$) with different cobalt concentrations of x = 0, 0.2, 0.35 and 0.5 were prepared by using a chemical co-precipitation method. A calcination temperature of 950 °C was used for all the synthesized samples. The X-ray diffraction analysis of the prepared samples clearly showed the formation of Barium hexaferrite. The dielectric properties (including dielectric constant, dielectric loss, tangential loss, and AC conductivity) of the samples were studied via an impedance analyzer. With increasing Co concentration, a significant increase in the dielectric constant, dielectric loss and tangential loss was observed. Saturation magnetization and coercivity of the prepared samples were measured using vibrating sample magnetometer (VSM). The VSM analysis showed a decreasing trend in the saturation magnetization and coercivity values with increasing the Co concentration. The magnetic coercivity was found to be 3567 Oe and 918 Oe for Co concentration of x = 0 and 0.5, respectively, which also showed changing of hard magnetic ferrite to soft magnetic ferrite.

Table of Contents

List of Figures

List of Tables

List of Abbreviations & Acronyms

Acronym	Meaning
BaM	Barium Hexaferrite
M_s	Saturation Magnetization
M_r	Remanence Magnetization
H_c	Coercivity
XRD	X-Ray-diffraction
SEM	Scanning Electron Microscope
VSM	Vibrating sample Magnetometer
CNT	Carbon nano tube
PEG	Polyethylene glycol
EVA	Ethylene Vinyl Acetate
EMI	Electromagnetic Interference
IICS	Institute of Industrial Control System
EM	Electromagnetic Wave
PP	Polypyrole
JCPDS	Joint Committee of Powder Diffraction Systems

Chapter 1

Introduction

1.1 Electromagnetic Interference Shielding

Electromagnetic interference (EMI) is a disturbance to an electrical circuit because of electromagnetic conduction or electromagnetic radiation from any other source [1]. It is also known as Radio Frequency Interference (RFI). EMI shielding has become a major concern especially in these days of vastly growing and progressing communication technology. It is a modern type of pollution, or we may call it electronic pollutants.

Initially, the EMI issue was concerned with military applications. But with the progress and development in this era in the communication sector, this has become a concern of normal society or of the common man [2]. Another reason for EMI is increased population causing excessive number and presences of electronic devices in close area to each other and due to upsurge in packing density of electronic assemblies in single equipment like mobiles sets, LCDs, Laptops, etc. It is providing a strong probability for electronic components and devices to become susceptible to undesired electronic emissions known as electromagnetic interference. This susceptibility can result in data disruptions, complete data loss, compromising of data quality, noise generation and damage to the device. So, in this perspective, it has become necessary to overcome this phenomenon of EMI [1]. To get rid of undesired electromagnetic emissions of electronic devices working in the close area, a shielding mechanism is to be introduced. Not only it is required to limit external EMI but self-generated interference of the device itself is to be controlled [3].

1.2 Materials for EMI Shielding

Electromagnetic interference shielding is done by using a suitable material that can act as a barrier between unwanted signals, which can interfere with a device. There are many different types of materials that are being used for EMI shielding applications [4]. This includes metallic alloys, composites of metals, ceramic materials, conducting

polymer composites, carbon containing materials, composites with polymers like epoxy and ferrites based composites [5]. Researchers are doing a lot of work in this field to overcome EMI by using different materials depending upon the environment and area of the application. This selection is also based on the material's response and at the frequency range in which material can provide shielding [2].

1.2.1 Metallic Alloys as Shielding Material

In the literature, metallic alloys have been reported as material for EMI shielding application. However, they have some unavoidable limitations. For example, Kesavapllai et al. synthesized polyol-derived Nickle (Ni) and Ni-Fe (Iron) alloys for the EMI shielding, which was proved a good candidate for this application within 12 GHz to 18 GHz. Problem with this alloy was disturbance of shielding properties of due to trapping of moisture during synthesis in Polyethylene glycol (PEG), used as dispersion media [6]. Keju et al. introduced Carbon Nano Tubes (CNTs) in Copper (Cu)-Ni alloy to get enhanced microwave absorption properties, but its porous structure was a drawback towards strength and durability [7]. In many other metallic alloys for the shielding application corrosion was a big issue [5].

1.2.2 Polymer Composite Based Shielding Materials

Composites from ethylene-vinyl acetate (EVA) copolymer have been used for the EMI Shielding. However, during processing, the viscosity of the polymer was very sensitive to control [8]. The transition metal oxides-based polyvinyl alcohol nanocomposites were also used for EMI shielding applications [2]. But here was a great drawback of rusting of metal. When the same composite was used in the form of coating, it damages due to poor wear resistance properties [9].

Conducting polymer composites were prepared using Polyaniline, Polypyrole (PP) Polythiophene for EMI shielding applications [10]. But the control of dielectric and magnetic properties of the material was difficult to achieve simultaneously in such type of conducting polymer composites. Both of these properties are important to the shielding mechanism of the material [11]. U type Barium hexaferrites ($Ba_4Co_2Fe_{36}O_{60}$) with epoxy composites were studied for their shielding properties, they could not show good performance in the 8 GHz to 12 GHz frequency range as shielding material [12].

1.2.3 Ferrites Based Shielding Materials

Ferrite-based materials have a great potential to use for EMI shielding purposes due to their enhanced electromagnetic wave absorbing properties [13]. They can fulfill the needs and overcome gaps like difficulties in the synthesis process, which were observed in making composite materials without using ferrites and can address the issues like strength and durability. An early experiment by J. Liu et al. in this regard of making core-shell composite with the coverage of polyaniline on the surface of Barium hexaferrite particle was performed which showed good properties of shielding within the range of X- Band or within GHz [14]. Therefore, ferrites took the attention of the researchers to be used for EMI shielding applications.

1.2.4 Doping of Ferrites with Different Cations

To get better magnetic properties for EMI shielding applications, the doping of the ferrites with different suitable transition metals has been reported in the literature [15]. In the start spinel ferrites, doped with Nickle Zinc (Zn) and Manganese (Mn) Zn were synthesized. They were tried in MHz frequency range, which proved them a good choice within this range. But they were not suitable for the GHz range due to their magnetic structure and coercivity values [16]. For this limitation spinel ferrites were not considered. Also, one reason for the failure of Spinel ferrites was the drop in complex permeability [17].

Another structure of ferrites called hexagonal ferrites was taken under research and experimentally they proved them very good choice and alternative of Spinel ferrites for EMI shielding material in the frequency range of 8 GHz to 12 GHz [12]. Hexagonal ferrites are strong candidates for EMI shielding applications due to improved properties like good chemical stability, higher values of permeability, high coercivity and cost-effectiveness [17]. And by doping suitable cations their magnetodielectric properties can be easily tailored as per requirement. These properties were not present in any other ferrite structure. So hexagonal ferrites are suitable as shielding material [18].

Hexagonal ferrites or hexaferrites makes a group of complex oxides in ternary system of magneto-plumbite structure AO-Fe_2O_3-MeO where A= Barium (Ba), Strontium (Sr), Calcium (Ca) and Me is divalent cation i.e. Zn, Copper (Cu), Ni, Cobalt (Co), Fe,

and Mn [12]. Keeping in view all these important aspects relevant to the properties of ferrites, Strontium hexaferrites were studied by substitution of Zinc Oxide (ZnO) [19]. But shielding properties of this material were not as much efficient as compared to properties of doped Barium hexaferrite with any transition metal. They also proved them good material within the 8 GHz to12 GHz frequency range by showing considerable attenuation of the unwanted signal by the reduction in values of magnetic parameters [19].

1.2.5 Doping of Barium Hexaferrites

Putting all focus on the frequency range of GHz, which is also a range of interest in our case, and to get justified behavior of material to prove it a good shield against EMI, M type hexaferrite, (Barium Hexaferrite) is currently being doped with transition metals. Doping is helpful in tailoring of magnetodielectric properties of Barium hexaferrite to encounter the phenomena of EMI. Doping of Ba^{2+}, or Fe^{3+} cations is normally done with transition metals like Neodymium (Nd), Manganese (Mn), Aluminum (Al), Magnesium (Mg), Cobalt (Co) as a substitution of Iron (Fe) Cation [20]. Because it is proved that such doping in Barium hexaferrite can produce desirable results. In a recent study, the Barium hexaferrite was doped with Nd. This doping showed the highest values of permittivity and permeability beside other synthesized materials and excellent shielding properties within the range of the 8 – 11 GHz [21].

On the other hand, the synthesis technique for doped Barium hexaferrite is easy, and the repeatability of results is confirmed [15]. By changing the concentration of dopants magnetodielectric properties are easily changeable. Synthesis techniques need no special environment i.e., high-temperature processing and special instruments. These issues were not easily controllable in other techniques [15]. By employing the sol-gel auto combustion method, response of Co and Lanthanum (La) doping was studied in Barium hexaferrite [13]. It caused the change in magnetic properties too. But their trend towards EMI shielding by studying dielectric properties was not studied [13].

The researchers also performed doping of ferrites using the coprecipitation method [22]. Barium hexaferrite was doped with Mn and Ni at different concentrations of dopants using the idea that when Ni and Mn were doped independently, they showed good properties as microwave absorbent material. By combined doping, improved

values were obtained based on dielectric and magnetic behavior. The coercivity of material changed from hard magnetic material to soft magnetic material when doped with Mn and Ni [23].

Following the trend of research at the start, many other researchers contributed their efforts in studying the magnetic or dielectric behavior of Co-doped Barium hexaferrite by replacing Iron (Fe). [20-21]. By doping of Co, the loss tangent was increased up to $32x10^{-3}$ from $0.5x10^{-3}$ in Barium hexaferrite. Also, values of relative permittivity were increased [22]. Similarly, a decrease in saturation magnetization value was observed when it was doped with Samarium (Sm) due to the difference in magnetic nature of Iron (Fe) and Zirconium (Zr) [26].

EMI shielding behavior of the Co-doped Barium hexaferrite by studying magnetodielectric properties have not been studied in great details. Studying Co-doped Barium hexaferrite for EMI shielding in different frequency ranges is a wide area. To fix the problem of working frequency range of Barium hexaferrite ferrite as an EMI shield, doping of Co in different concentration can be helpful. Therefore, the composition which is suggested in present research work is to make Barium hexaferrite capable to work as EMI shield within GHz frequency range. This composition has not been studied previously. Studying Co-doped Barium hexaferrite with suggested composition will be useful to reduce resonance frequency at lower level of microwave range by reduction in magnetic anisotropy field. This composition will make it efficient shield against EMI within GHz frequency range [17].

1.3 Objectives of this Work

This research work has the following objectives:

- Employing coprecipitation method for the Synthesis of Co-doped Barium hexaferrite at different concentrations (X) of Co at X=0.0, 0.2, 0.35, 0.5.
- Characterization of the synthesized materials using X-Ray Diffraction (XRD), Scanning Electron Microscopy (SEM), Vibrating Sample Magnetometer (VSM) and LCR meter.
- To get the improved magnetodielectric properties of Barium hexaferrite by Co doping.

Chapter 2

Literature Review

2.1 Magnetism

Magnetism is the ability of the material to respond to any externally applied magnetic field [27]. Upon interaction with this external magnetic field, orientation and alignment of dipoles of the material change. This change of orientation of dipoles depends upon the class of the material from which it belongs. So, we can classify the magnetic materials based on orientation and alignment of their magnetic dipoles relative to each other. Different classes of magnetic materials are discussed below [28]:

2.1.1 Diamagnetic Materials

In diamagnetic materials, when the magnetic field is applied, orbital motion of the electrons gives rise to diamagnetism. Orbital motion is responsible for the generation of the magnetic field which opposes the applied magnetic field. Electrons of the atom of diamagnetic material tend to counteract externally applied fields by aligning them in direction opposite to applied magnetic field (Fig. 2.1). Therefore, the net magnetic moment of an atom is zero in case of diamagnetic materials. As soon as the magnetic field is removed, magnetization in these materials again drops down to zero. Actually, thermal intrinsic energy is higher than the potential energy which aligns the dipole and dipole moments tend to randomize due to thermal agitation. Examples of some diamagnetic materials are Copper, Gold, Silver and Mercury [27].

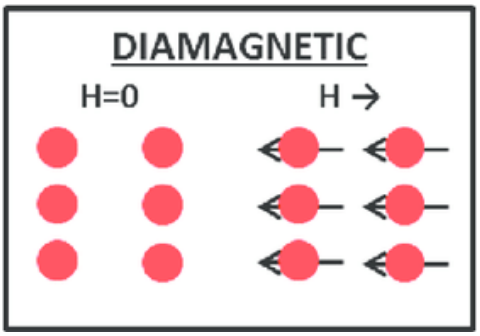

Fig. 2.1: Ordering of dipoles in diamagnetic materials [29]

2.1.2 Paramagnetic Material

Magnetic dipole moment, associated with few atoms, ions or molecules present in the solid, is permanent in paramagnetic materials. In the absence of magnetic field (H = 0), the net magnetic moment associated with each atom is zero due to random orientation (Fig. 2.2). In the presence of applied magnetic field, alignment of dipole occurs in the direction of applied field (Fig. 2.2). When H (magnetic field) is applied dipoles are aligned in direction of the field, hence the magnetic susceptibility (χ_m) become positive; $\chi_m > 0$. Examples of some paramagnetic materials are Aluminum, Sodium and Titanium [27].

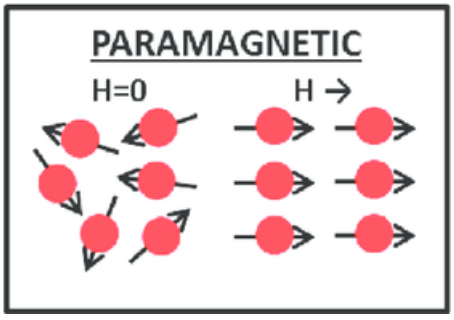

Fig. 2.2: Ordering of dipoles in paramagnetic material [29]

2.1.3 Ferromagnetic Material

In ferromagnetic materials, movement of electron pairs in atomic or molecular orbitals results in formation of magnetic dipoles. These dipoles align themselves even in the nonappearance of externally applied magnetic field causing the phenomena of ferromagnetism (Fig. 2.3). Materials having partially filled valence bands/shells usually exhibit this phenomenon and form permanent magnets. Dipoles are aligned in

domains and these domains are aligned opposite to each other in bulk of a material resulting in zero net magnetic moments throughout the material. Examples of ferromagnetic materials are Iron, Cobalt and Nickel [27].

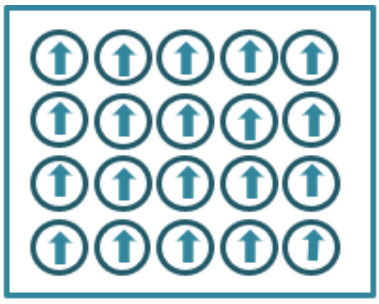

Fig. 2.3: Ordering of dipoles in ferromagnetic material [27]

2.1.4 Ferrimagnetic Material or Ferrites

Ferrimagnetism is form of permanent magnetization shown by some of ceramic materials. In ferrimagnetic materials, cations, occupying different crystallographic sites, experience antiferromagnetic coupling and the magnetization of two sublattices is opposite to each other (Fig. 2.4). But net magnetization is non-zero because of unequal strength of the two magnetizations. These materials are of great interest a due to special properties they are highly suitable for high frequency applications and in special magnetic devices.

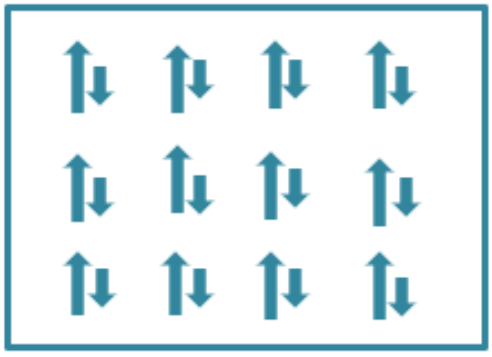

Fig. 2.4: Ordering of dipoles in ferrimagnetic materials [27]

2.1.5 Antiferromagnetic Material

Anti-ferromagnetism is a phenomenon in which two dipoles arrange themselves in opposite or antiparallel directions (Fig. 2.5). The net magnetization is zero because magnitude of all dipoles is equal. This antiparallel arrangement occurs at a critical temperature called Neel's temperature at which magnetic susceptibility has a maximum value and after this temperature magnetic susceptibility decreases [27].

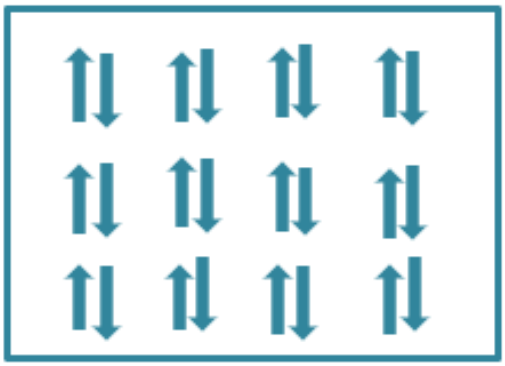

Fig. 2.5: Ordering of dipoles in antiferromagnetic material [27]

2.2 Magnetic Properties of materials

Magnetic Materials have some important magnetic properties including coercivity, saturation magnetization, remanence magnetization. These properties can be studied and measured using Hysteresis curve. On the basis of these properties, they can further be classified as soft and hard magnetic materials. Magnetic properties and classes are discussed in coming section later on. But before proceeding to that discussion on Hysteresis curve seems natural.

2.2.1 Hysteresis Curve

The Hysteresis curve or loop is basically a graph plotted between magnetic moments per gram at Y-axis and applied magnetic field (H) at X-axis. On the basis of variation in the magnetization of material in response to applied magnetic field, graph is plotted to study some important properties. Here in Fig. 2.6, M_S, M_r and H_c are saturation magnetization, remanence magnetization and coercivity respectively. The spread of the Hysteresis curve tells us that whether the material is a soft or hard magnetic

material. The area of the Hysteresis curve is a measure of energy loss due to the dissipation of energy required to move the domain walls back and forth [27].

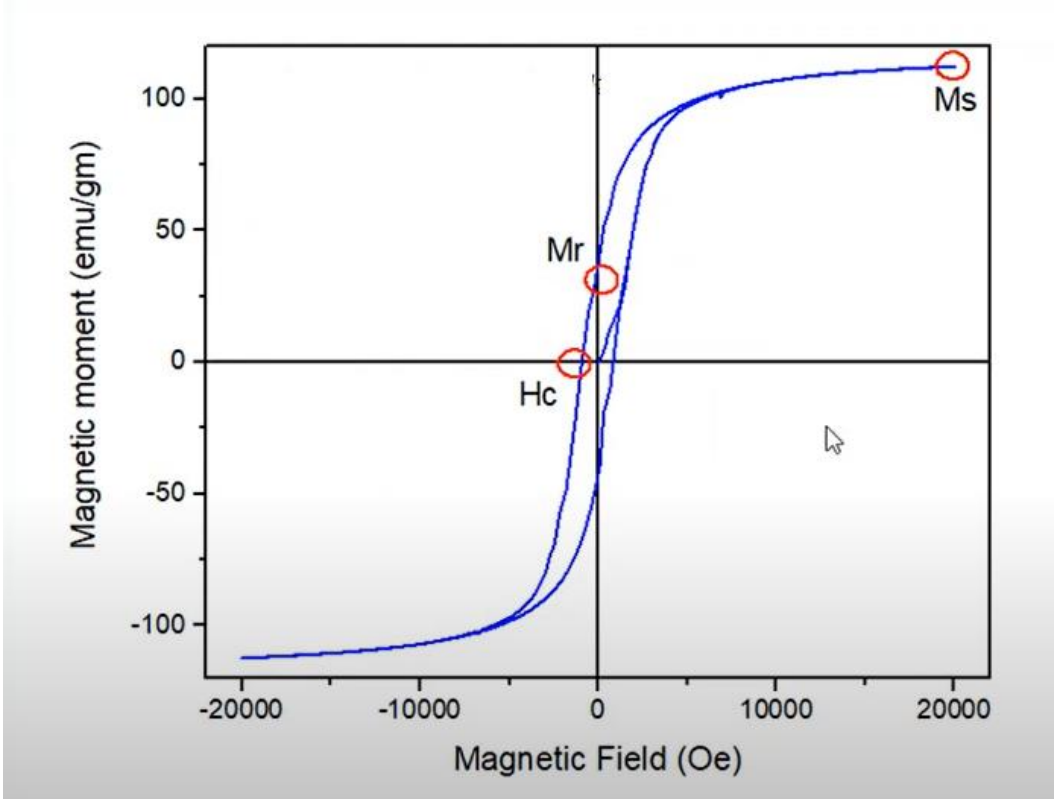

Fig. 2.6: An exemplary Hysteresis curve [27]

2.2.2 Saturation Magnetization

When magnetization of material reaches a maximum and it does not increase further, by increasing magnetic field which is applied externally, maximum obtained value of magnetization at this point is known as saturation magnetization. The unit of saturation magnetization is KA/m. In Table 2.1 few elements are mentioned against their saturation magnetization (M_s) value for better understanding.

Table 2.1: Elements with saturation magnetization values [27]

Name of the element	**Saturation Magnetization KA/m**
Iron	1.38×10^5
Cobalt	1.15×10^5
Gadolinium	1.64×10^5

2.2.3 Remanence Magnetization

When a material is placed in magnetic field (H), it attains some value of magnetization. When this applied magnetic field becomes zero, magnetization of material has a non-zero value of magnetization. This nonzero value of magnetization is known as remanence magnetization (M_r) (Fig. 2.6). This property is important in a sense to measure magnetization of material in absence of any applied magnetic field.

2.2.4 Coercivity

To completely demagnetize a material, or to bring remanence magnetization to zero value, a negative direction field to already applied field is to be applied. The maximum value of that applied field in negative direction is known as coercivity with units of Oe. It is also known as coercive force of the material. It can also be defined as external applied field in reverse direction to completely demagnetize a permanent magnet. At this stage H becomes equal to $-H_c$ (Fig. 2.6). This property is very important as it helps to decide whether a material is hard or soft magnetic material.

Hard magnetic materials have higher value of coercive fields, whereas soft magnetic materials have low values of coercive fields. So, on plotting hysteresis curves of both materials, hard magnetic material would have higher value of coercivity with large are of the loop and vice versa.

2.3 Dielectric Response of Materials

Dielectric behavior of material is governed by response of the electron of material to applied electric field in terms of polarization [30]. There are different types of

polarization which take place in dielectric materials when they interact with the applied field. These interactions are discussed in detail below [27].

2.3.1 Electronic Polarization

When the dielectric material is positioned within the electric field, the electron cloud of atoms is displaced relative to nuclei in atom, which produces an induced dipole moment in the molecule. Due to the absence of ionic or permanent dipoles in a dielectric, the polarization is only due to electronic polarization. Inert gases and elemental dielectrics such as diamond can show such type of polarization [27].

2.3.2 Ionic Polarization

Ionic polarization takes place in solids with ionic bonding having dipoles. If some symmetry in crystal structure is present, but these dipoles get cancelled. In the presence of applied electric field positive and negative ions are displaced from their equilibrium positions hence inducing dipole moment. Alkali halides can show such type of polarization [27].

2.3.3 Dipolar and Orientation Polarization

It is only applicable to the polar dielectric materials. When no any electric field is applied, orientation of dipoles is random. So, the sum of their dipole moment is zero. When these polar dielectric materials are placed within the electric field, rotation of dipoles causes to align them in the direction of electric field. Ceramics, inorganic oxides and polymers are the few dielectrics to show such type of polarization [27].

2.3.4 Interface and Space Charge Polarization

Space charge polarization takes place due to the diffusion of ions along with applied electric field. It usually occurs due to the gathering of charges in the at the grain boundaries of material. This type of polarization can be observed in doped ferrites [27].

2.4 Dielectric properties:

Dielectric properties mainly include dielectric permittivity (dielectric constant, dielectric loss), tangent loss, ac conductivity, and electric modulus. These Properties play an important role towards EMI shielding application of materials if are suitable [22]. Also, the information about the formulation of electric field in the material can be gained from these properties. Here incoming sections, an overview of these properties will be given for better understanding.

2.4.1 Dielectric Permittivity

In an electric field, capability of material to polarize is known as permittivity. It can be explained with the help of equation

$$\varepsilon_r = \varepsilon' + i\varepsilon'' \quad \text{(2.1)}$$

Where ε_r represents dielectric permittivity of a medium, ε' and ε'' are the real and imaginary parts of it. Real part, dielectric constant represents the storage capability of electromagnetic energy (EM), whereas imaginary part known as dielectric loss deals with thermal conversions. The main reason for the dielectric loss is the lag of response of dielectric material to the applied electric field. Dielectric constant can be calculated using formula

$$\varepsilon' = Ct/\varepsilon_0 A \quad \text{(2.2)}$$

Where ϵ' is permittivity of material which represents its ability to store charge, capacitance in farad is denoted by C, thickness in meter is given by t, cross-sectional area of the flat surface of the pellet is given by A and ε_o is the constant of permittivity of free space with a value equal to 8.85×10^{-12} F/m.

The imaginary part that corresponds to calculation of the energy dissipation using the following equation 2.3:

$$\epsilon'' = \acute{\varepsilon} \times D \quad \text{(2.3)}$$

Where $\epsilon''$is dielectric loss of material and D represents the dissipation factor and ϵ' is permittivity of material which represents its ability to store charge [30].

2.4.2 Dielectric Tangential Loss

Ratio of dielectric constant and dielectric loss dielectric tangent loss is termed as dielectric tangent loss. The following formula given in equation 2.4 can be used in calculation of tangential loss.

$$\tan\delta = \frac{1}{\omega\varepsilon_o\rho} \quad (2.4)$$

where ω=2πf, f is a frequency of applied field, ε_o is a permittivity of free space and ρ is a resistivity.

2.4.3 AC conductivity

Conductivity is the physical property of a material which characterizes the conducting power inside the material. It can be calculated using equation 2.5.

$$\sigma_{ac} = \omega\varepsilon_o\varepsilon'' \quad (2.5)$$

Where ω=2πf, f represented the frequency, ε_o represents the permittivity of free space and ε″ represents imaginary part of dielectric permittivity. According to literature, the total conductivity is calculated by following relation given below in equation 2.6 [31].

$$\sigma_{tot} = \sigma_o(T) + \sigma(\omega, T) = \sigma_o(T) + B\omega^s \quad (2.6)$$

where $\sigma_o(T)$ represents DC conductivity which is frequency independent and occurs due to band conduction. $\sigma(\omega, T)$ represents ac conductivity. Hopping process among ions of same element due to present in different valence state is responsible for this conductivity [32]. B and s are temperature dependent constants. They also depend upon composition.

2.5 Conductivity in Ferrites:

Owing to the distinct electrical properties of ferrites, they are applicable for various electronic applications. The conduction mechanism in ferrites differs from semiconductors as in ferrites the temperature affects the charge carrier mobility in turn effecting the conduction mechanism. Charge carriers in ferrites are localized at the

magnetic atoms and carrier concentration in independent of temperature. Hopping of 3d electrons between Fe^{+2} and Fe^{+3} causes the conduction in ferrites. Closely packed oxygen anions surround the metal cations causing the isolation of electrons to a particular ion and there is a small overlapping of anionic cloud or orbital. Due to the isolation of each electron to a particular ion, localized electron model is more significant in ferrites as compared to band model [30].

2.6 Introduction to Ferrites

Ferrites, also known as ceramic powders, are non-conductive, hard, brittle and are generally related to the class of mixed oxides of iron in which iron is usually substituted with rare earth elements like Barium, Strontium, and some metallic elements like Co, Ni Mn, Mg, and Cu. Ferrites have always been of strong interest owing to their distinct electrical, magnetic and microwave absorption properties [21]. The magnetic behavior of ferrites depends on composition as well as on microstructure including pore size distribution and grain boundaries. Depending upon the magnetic coercivity, ferrites can be classified as “Soft” and “Hard” ferrites [33].

2.6.1 Soft Magnetic ferrites

Those ferrites which can easily be magnetized and demagnetized by the applying and removing of applied field are placed in class of soft ferrites. They can only remain magnetized when they are under the influence of magnetic field. For soft ferrites, the area of hysteresis loop and coercivity value is very low. This means that the material magnetization can easily be reversed without losing much energy. An ideal ferrite would have

- Low value coercivity
- Large value of saturation magnetization
- Zero value remanence
- zero hysteresis loss value
- Large permeability

2.6.2 Hard ferrites

Hard ferrites are also known as Ceramic Magnets. Magnetization of hard ferrite material remains retained even after the removal of applied field. They have a large hysteresis loop as well as high value of coercivity. Oxides of Iron, Barium and Strontium show behavior of hard ferrites.

2.7 Magnetic Properties of Hexaferrites

Magnetic properties like coercivity (H_c), saturation magnetization (M_s) and remanence magnetization (M_r) of hexagonal ferrites can be altered by the addition of metallic cations by doping. With the addition of metallic cation like Aluminum, Co, Gallium or Chromium, the magnetic anisotropy and magnetization of Barium hexaferrite can be changed. This change can help to decide the application of material. Materials with high values of coercivity is useful for recording media, having low values of coercivity can make a material useful in EMI shielding applications [17].

Out of large metallic ions, like Barium and Strontium, the size of crystal lattice is varied which forms the basis of magneto-crystalline anisotropy resulting in distinct magnetic properties in hexaferrites. The magnetization in most of the hexagonal ferrites is shown in the direction of c-axis because of which their XRD pattern differs from any other ferrites oriented in random order [2].

2.8 Application of Ferrites

Possessing some special characteristics ferrites are suitable for many important applications in power conditioning, electromagnetic devices, electromagnetic wave absorbers (Shields), magnetic inks for bank cards, and recording media etc. [34]. Some of the major fields of applications of ferrites are listed below.

- Electromagnetic interference shielding
- Drug delivery
- Magnetic shielding
- Magnetic sensors
- Pollution control
- High frequency applications

2.9 Classification of Ferrites.

The dominant compound in ferrites is Fe_2O_3. The ferrites can be classified based on this compound, as following:

- Spinel Ferrites (Cubic)
- Garnet
- Ortho Ferrites
- Hexaferrites

The molar ratio of Fe_2O_3 to other oxide components in these ceramic compounds help to identify different classes of ferrites as shown the table 2.2:

Table 2.2: Classes of ferrites [35]

Type	**Molar Ratio**	**Terms Used For**
Spinel	Fe_2O_3.MeO	MeO represents Transition Metal Oxide
Garnet	$5Fe_2O_3.3Me_2O_3$	Me_2O_3 represents rare earth metal oxides.
Ortho	$AFeO_3$	A represents rare earth metal like HO, Dy, Er, Yb, Y
Hexaferrite	$6Fe_3O_4$.1MeO	MeO represents a Divalent metal oxide from group IIA. For example, BaO, CaO, SrO

2.9.1 Spinel Ferrites

Crystal structure of Spinel ferrite can be presented by AB_2O_4. A is a divalent cation and B is trivalent cation. Examples of divalent cation include Co^{2+} Ni^{2+} Zn^{+2} Mn^{+2}, Mg^{+2} and trivalent cation can be iron or aluminum, etc. The crystal structure of spinel ferrite is acquired from $MgAl_2O_4$, a mineral spinel. The unit cell structure of these spinel ferrites is cubical, and each unit cell contains eight smaller unit cells which are called octanes or formula units. Each unit cell is comprising of 32 oxygen atoms,

forming a lattice which is face-centered cubic in structure with tetrahedral and octahedral sites (Fig. 2.7) & (Fig. 2.8). Tetrahedral sites are denoted by A sites, and they are surrounded by four oxygen atoms while six oxygen atoms surround the octahedral sites, represented as B sites. The spinel ferrite structure is not electrically neutral because when metal ions of valency of either +2 or +3 are filled in A and B sites, positive charge dominates [36].

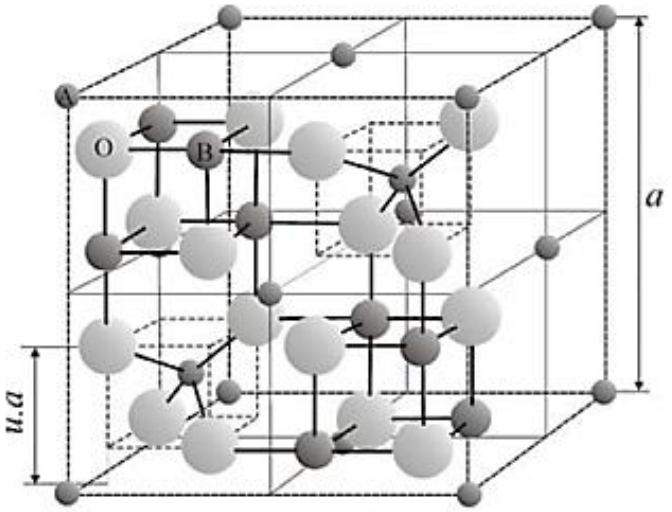

Fig. 2.7: Face centered cubic unit cell of Spinel structure with four formula units: Tetrahedral-A sites are represented by small sphere; Larger spheres represent the Octahedral B site and Oxygen atoms are represented by largest spheres [37].

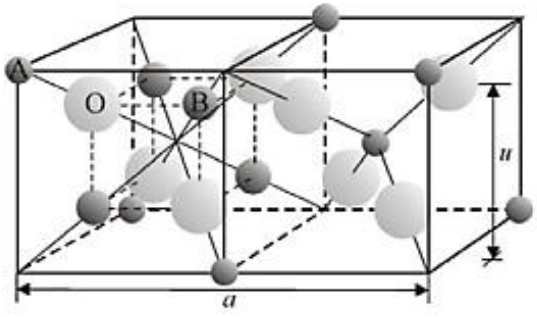

Fig. 2.8: Two Adjacent formula units of spinel structure [37]

2.9.2. Garnets

Garnets are the second group of ferrites with the general formula $Me_3B_5O_{12}$ where A represents a rare earth metal cation like yttrium where B represents iron. The unit cell of garnet ferrites is cubical, and it contains eight smaller formula units. In garnet, ferrites are comprised of Tetrahedral A sites, Octahedral B sites and Dodecahedral C sites. A and B sites have distribution of iron cations (Fe^{3+}) shown in red color in the ratio of 3:2 while dodecahedral C sites are occupied by Me cations which is Yttrium shown in grey color, surrounded by the oxygen atoms shown in white color (Fig. 2.9). Garnet is known for its optical transparency and for their magneto-optical applications [38].

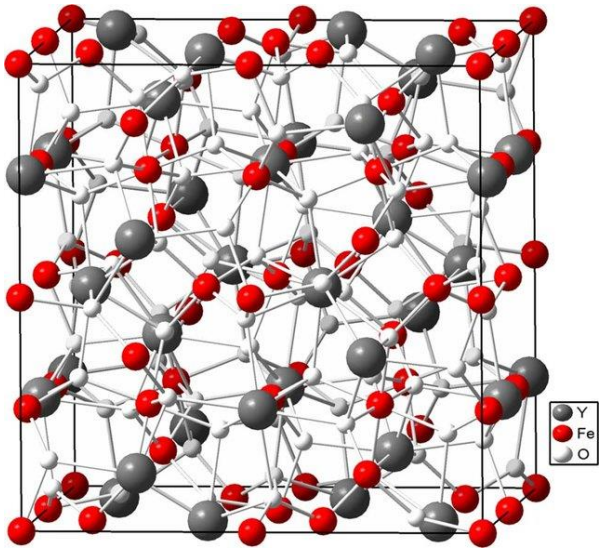

Fig. 2.9: Representation of Yttrium and Iron Garnet (YIG)

2.9.3 Ortho Ferrites:

Orthoferrites are the third group of ferrites with distorted perovskite structures having a common formula of ABX3. A is a rare earth or alkaline metallic cation, B presents transition metal cation, usually Fe and X is anionic species, which is oxygen, in most cases. In orthoferrites, an octahedron is formed by Fe, being the central ion and coordinated by six oxygen atoms. The interstitial sites in octahedral structure are filled by the A cations coordinated by 12 oxygen atoms. Ortho ferrites are known for their high domain wall velocities and have applications in magnetic field sensors, communication techniques and electronic current [39].

2.9.4 Ferrites with Hexagonal Structure:

Hexaferrites belong to the fourth class of ferrites having hexagonal structure. These were first discovered in the 1950s and developed over the past several decades. Hexaferrites based on Barium, Strontium, and Calcium along with Iron possess high coercivity and permeability values and can conduct magnetic flux well. This polycrystalline ferrite attained considerable attention field electronic industry because of its less cost, easy engineering, and remarkable magnetic properties. Hexaferrites can be further be placed into different classes named as: M, U, W, X, Y and Z. Structural stacking and molecular formula against each type of hexagonal ferrite is given in Table 2.3 below [34].

Table 2.3: Formula and types of hexagonal ferrites

Hexagonal Material	**General Formula**	**Stacking Sequence**
M Type	$BaFe_{12}O_{19}$	RSR*S*
Y Type	$Ba_2Me_2\ Fe_{12}O_{22}$	TSTSTS
W Type	$BaCo_2\ Fe_{16}O_{27}$	RSSR*S*S*
Z Type	$Ba3Co2Fe_{24}O_{41}$	RSTSR*S*T*S*
X Type	$Ba_2Co_2Fe_{28}\ O_{46}$	RSR*S*S*
U Type	$Ba_4Co_2Fe_{36}\ O_{60}$	RSR*S*T*S*

To the interest of this research work all focus will be on M type hexaferrite. So, in coming sections M type Hexaferrite will be studied in detail.

Crystal Structure and Composition of Hexaferrites

Hexaferrites obey the formula $MO+MeO/Fe_2O_3$ where M corresponds to the metals like Barium, Strontium, Calcium etc. Me represents transition metal cation like Iron, Cobalt, Manganese etc. There is a close packing of Oxygen ions layer in the crystal structure of hexaferrite and any divalent of trivalent metal cation reside in the interstices of the structure. Substitution of heavy metal ions like Ba or Sr occur in the oxygen layers. In hexaferrites, there are essentially 3 fundamental structural blocks names as: S, R and T and they have a rotational symmetry at 180^o around the hexagonal c axis represented as S*, R* and T* respectively (Fig. 2.10).

A neutral (RS) block with the total composition of $MFe_{12}O_{19}$ (M Phase) is formed when R subunit combines with S^{+2}. Similarly, a neutral TS can be formed when T subunit combines with S0 with total composition of $Ba_2Me_2Fe_{12}O_{22}$, called as Y phase. Likewise, different composition like X, Y, Z, W, and U can be formed by varying the stacking sequences of hexagonal and cubic units [40].

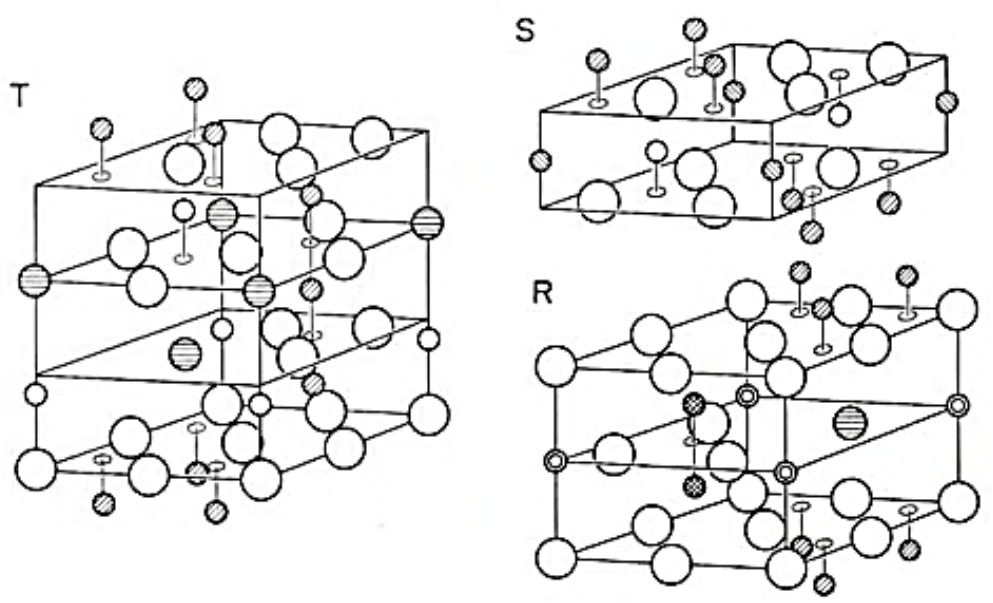

Fig. 2.10: Representation of fundamental blocks S, R and T in hexaferrites

2.10 M Type Barium Hexaferrite

The most commonly produced magnetic material is M type hexaferrite. It has a melting point of 1390 ^{o}C with magnetic coercivity of 160-255 KAm^{-1} [17]. Ferroxdure or BaM are the other names of M type Barium hexaferrite. Barium hexaferrite found its usage in magnetic recording media, permanent magnets, and in microwave devices [17].

2.10.1 Crystal Structure of M-type Barium Hexaferrite

The composition of fundamental structural R and S blocks in Barium hexaferrite is $BaFe_6O_{11}$ and Fe_6O_8 respectively. R and S blocks are stacked in M type Barium hexaferrite to form a unit cell in sequence RSR*S* where the sign star denotes the 180^{o} rotation about the c-axis of the hexagonal lattice (Fig. 2.11).

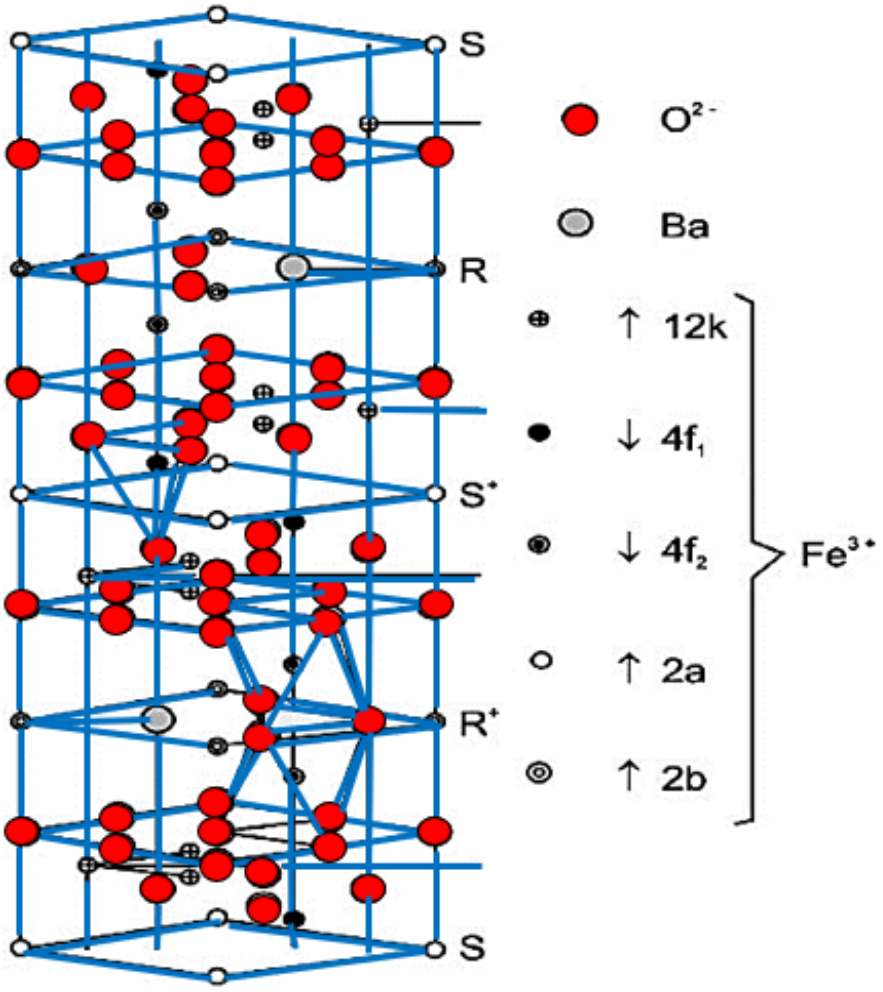

Fig. 2.11: Spin orientation of sublattices in unit cell of BaM [40]

It is also clear from Fig. 2.11 that two $BaFe_6O_{11}$ molecules are present in the unit cell of Barium hexaferrite (BaM). Four oxygen ions are present in each of the two hexagonal layers in S Block while R block constitutes three hexagonal layers of oxygen. One oxygen ion in the middle hexagonal layer in R block is replaced by a Barium ion. Five interstitial sites are occupied by the metal ions in the unit cell of Barium hexaferrite. The location of these sites, their sublattices, number of ions and coordination's are mentioned in the Table 2.4 below:

Table 2.4: Location, sublattices and coordination of interstitial sites in Barium hexaferrite [2]

Block	Sublattice	Coordination	Ions per unit cell	Direction of Spin
S Block	$4f_1$	Tetrahedral	4	Downward
	2*a*	Octahedral	2	Upward
R Block	$4f_2$	Octahedral	4	Downward
	2*b*	Bi-pyramidal	2	Upward
S-R Block	12*k*	Octahedral	12	Upward

2.11 Methods for Synthesis

Methods normally used for the synthesis of ferrite nanoparticles are as follows [41].

- Co-Precipitation
- Sol-Gel Method
- Mechanical Alloying Technique
- Combustion Flame Synthesis
- Sono-Chemical Method
- Hydrothermal Method
- Micro Emulsion Method
- Solvothermal

In the present work, the Barium hexaferrite nanoparticles were prepared using the chemical co-precipitation method. Therefore, in the following section, only this technique will be briefly discussed

2.11.1 Co-precipitation method

The formation of mixed crystal due to precipitation of a soluble component of solution with a macro component of the same solution is known as co-precipitation [42]. Precipitation is a classical and easiest method to synthesize ferrites nanoparticles. The use and selection of a suitable precipitating agent is necessary for precipitation to occur. Also, this method is very much sensitive to pH. This technique provided better control on products and is cost effective. This method can be used for massive production and is cheap process as it needs no special equipment or instrument. During this process, no elevated temperature treatment is required hence it needs no special instrument or oven/furnace. The materials or precipitate which was made through this technique have wide applications in different fields including EMI shielding application [41].

Advantages of Co-precipitation

Advantages of co-precipitation method are given below:

- Cheap/economical method
- It is very simple method, no complex route
- Reproducibility is confirmed
- A time saving method
- No specially controlled environment is required
- Extraordinary high temperature is not required for process
- Good for massive production
- Easily controllable
- Not as much hazardous as other techniques can be
- No special equipment and apparatus are required
- Good for massive production
- Suitable synthesis method for applications like EMI shielding

Disadvantages of Co-precipitation

This method has some disadvantages too as given below.

- Inhomogeneity of particle size
- Inclusion of impurities at different processing stages
- It is very much sensitive to pH
- This method is not useful for some specific applications like recording media

Its advantages over disadvantages are more enough to make it one of the best choose route for the synthesis of nanoparticles [43].

Chapter 3

Experimental Procedure & Characterization Techniques

3.1 Materials

In the synthesis of Barium hexaferrite the chemicals were of purity ≥ 99%. They were used without any further purification. The solutions were prepared in demineralized water (DM water). Suppliers of the chemicals were Unichem and Sigma Aldrich. Detail of chemicals used in process can be seen in Table 3.1 below.

Table 3.1: List of chemicals used in synthesis of Barium hexaferrite

S. No.	Name of Chemical	Formula	Molecular Weight
1	Barium Nitrate	$Ba(NO_3)_2$	261.36 g/mol
2	Iron Nitrate nonahydrate	$Fe(NO_3)_3.9H_2O$	404 g/mol
3	Cobalt Nitrate hexahydrate	$Co(NO_3)_2.6H_2O.$	291.04 g/mol
4	Sodium Hydroxide	NaOH	39.997 g/mol

3. 2 Experimental Details

By using the co-precipitation method, various samples of the Barium hexaferrite were prepared. The samples of the Barium hexaferrite were doped in the following different concentration x of Cobalt:

- x = 0.0
- x = 0.2
- x= 0.35
- x = 0.5

Mass of solutes were calculated using formula given in equation 3.1:

$$mass\ (g) = \frac{molarity\ X\ molecular\ mass\ X\ 200}{1000} \ldots\ldots\ldots\ldots\ldots\ldots (3.1)$$

The detailed synthesis of the samples is discussed in the following section.

3.2.1 Synthesis of Barium Hexaferrite

For better understanding of the experimental procedure of synthesis of Barium hexaferrite, a flow chart is shown in Fig. 3.1.

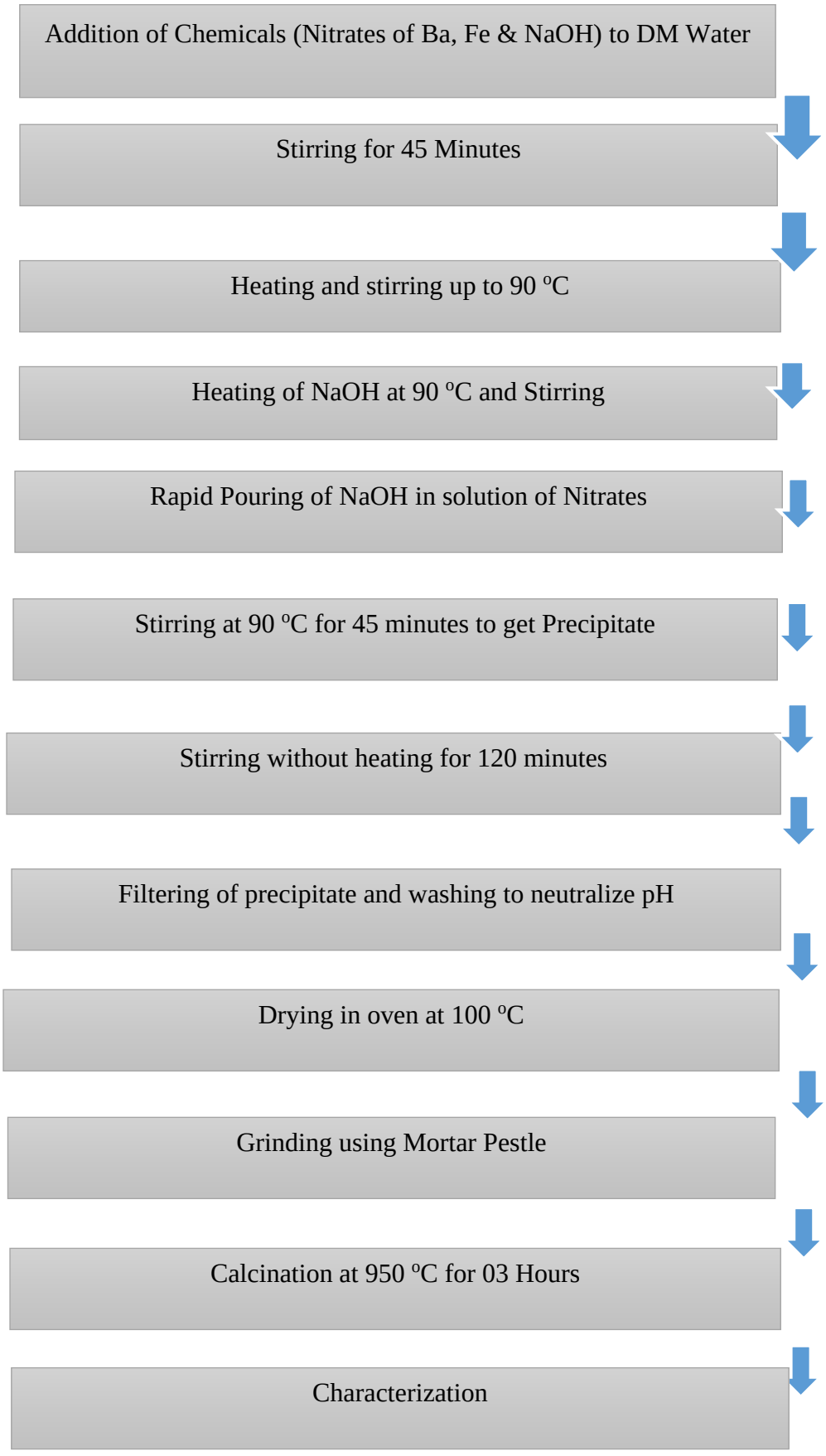

Fig. 3.1: Flow Chart of Co-Precipitation method for synthesis of $Ba_{(1-x)}Fe_{12}(Co)_xO_{19}$

Solutions of Barium nitrate Ba $(NO_3)_2$ and Iron nitrate nonahydrate Fe $(NO_3)_3.9H_2O$ were prepared according to their stoichiometric ratios. Ba $(NO_3)_2$, Fe $(NO_3)_3.9H_2O$ were dissolved in 200 ml of Demineralized water (DM water) separately by constantly stirring using a magnetic stirrer for 30 minutes for their complete dissolution and to get a clear solution in water. Later, 200 ml of DM water was taken to dissolve Sodium hydroxide (NaOH) and was stirred until solution get cleared and complete dissolution took place. In a one-liter beaker, both solutions of nitrates of Barium and Iron were added with continuous stirring using a magnetic stirrer for 45 minutes. The solution was heated up to 90 °C with continuous stirring (Fig. 3.2).

Figure 3.2: Stirring and heating of chemicals

Simultaneously on the other stirring hot plate Sodium hydroxide (NaOH) was mixed and its temperature was raised to 90 °C. As the solution of nitrates and NaOH reached at 90 °C, rapidly 200 ml of NaOH was decanted into the beaker containing solution of nitrates, Barium nitrates (Ba $(NO_3)_2$) and Iron nitrate nonahydrate (Fe $(NO_3)_3.9H_2O$) with continuous stirring.

The formation of precipitate was observed with light brown color particles at the same instance. Stirring was continued for 45 minutes maintaining the temperature of the solution at 90 °C. Later on, the heating was switched off but stirring was carried out for 2 hours. Then solution was allowed to cool and settle down further. With help of filter paper, solid precipitate was washed many times with DM water to achieve its pH value up to 7. Initially its pH value was about 11 and it was highly basic in nature. The co-precipitation method is highly sensitive in this respect. So extra care was done to bring the precipitate to neutral pH level. After this neutral filtrate was dehydrated in drying oven at 115 °C for three hours. A dark-colored precipitate in solid formed like cake. This cake was ground using mortar pestle. After grinding it appeared as a dark brownish powder (Fig. 3.3).

Fig. 3.3: Synthesized Barium hexaferrite after drying

This powder was then calcined at 950 °C in a furnace and then was furnace cooled. Later on, it was further ground to get the final product (Fig. 3.4).

Fig. 3.4: Synthesized powder obtained after calcination

3.3 Characterization Techniques

The synthesized samples were characterized by using X-Ray Diffraction (XRD), Scanning Electron Microscopy (SEM), LCR meter and Vibrating Sample Magnetometer (VSM). Brief detail on equipment and samples prepared for the characterization are given in the following sections:

3.3.1 X-Ray Diffraction Technique

XRD is the backbone of material sciences and engineering which is helpful for the identification of the degree of crystallinity and structure of a material by changing the linear information of crystal lattice into angular information. In this technique, X-rays are used as a probe due to their comparable wavelength to interatomic spacing. These X-rays are incident on the plane of atoms of material which are diffracted from the atoms (Fig. 3.5). When two different beams diffracted from planes constructively interfere, a high intensity peak as a signal on monitor is observed. This peak shows the presence of any plane in that material at that specific angle.

The principal of this technique is given in equation 3.1, known as Braggs Law.

$$n\lambda = 2d\sin\theta \quad \text{.....(3.1)}$$

Here in equation 3.1

n = Order of interference

θ = Incidence angle

d = Interlayer distance

λ = Incident X-ray wavelength

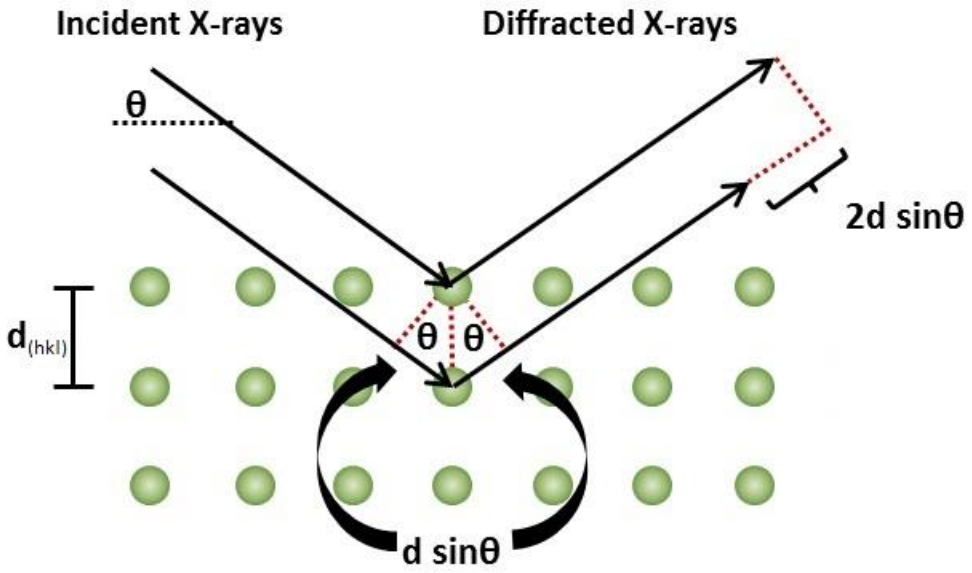

Fig 3.5 Incident X-ray Beam Scattered by Atomic Plane in a Crystal [44]

In the present work, the JEOL-JDX-9C X-ray diffractometer was used. The XRD data were analyzed to investigate crystal structure, lattice parameters and particle size. After scanning the sample on an X-ray diffractometer and obtaining d- values, the next step was to identify the phase. By using different software or manually, can perform this task using the standard library of Joint Committee of Powder Diffraction System (JCPDS) data cards [45].

Calculation of particle size and lattice parameters

Lattice parameter is the edge-to-edge length of the cell. It can also be termed as lattice constant. For a hexagonal system as in our case the following formula in equation 3.2 can be used for the calculation of lattice parameter [34].

$$\frac{1}{d^2} = \frac{4}{3}\left(\frac{h^2+hk+k^2}{a^2}\right) + \frac{l^2}{c^2} \quad \ldots\ldots\ldots\ldots (3.2)$$

In the above equation 3.2, lattice constant is "a", the wavelength of X-ray radiation is 1.54 for Cu-kα radiation, and miller indices are h, k, l.

Debye Scherrer formula in equation 3.3 is used to calculate particle size.

$$D = 0.9\,\lambda/\beta\,cos\theta \quad \ldots\ldots\ldots\ldots\ldots\ldots\ldots\ldots\ldots\ldots\ldots\ldots (3.3)$$

Here, λ represents the wavelength of X-ray used, θ and β represent angle of diffraction and full width half maxima (FWHM) respectively.

3.3.2 Scanning Electron Microscopy (SEM)

SEM can be used to examine the surface morphology of the specimen under test. On irradiation of specimen by high energy electron beam, interactions between incident electron beam and the constituent atoms of the specimen arises different type of signals as shown in the Fig. 3.6. Secondary electrons and back scattered electrons (BSE) help to visualize the surface morphology of the specimen along with elemental analysis to know the composition (Fig. 3.6)

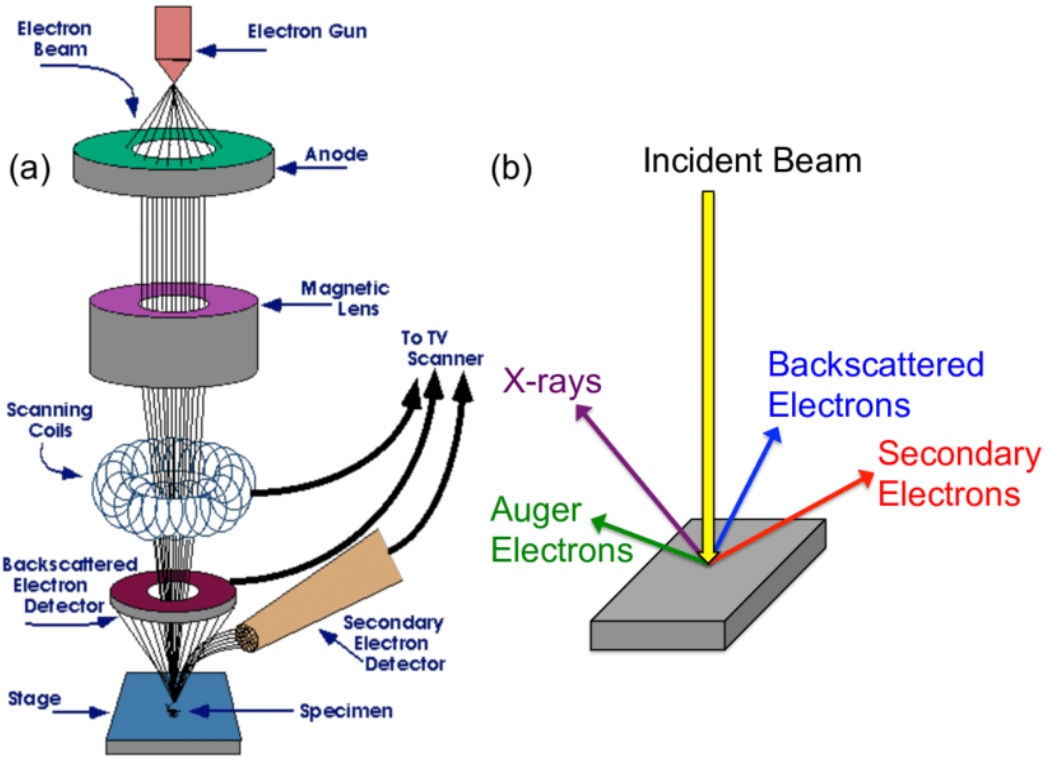

Figure 3.6: Schematics and emission of various signals from specimen [46]

In the present work, the surface morphology of the synthesized samples was studied via JEOL JSM-5910. For SEM studies, a suspension using Ethanol was prepared for each sample. The sample was taken in a very small amounts to prepare the suspension. Then with the help of a capillary tube, this suspension was dropped on a Cu stud and then dried by placing at room temperature.

3.3.3 LCR Meter

LCR meter is named LCR because it can measure Inductance (L) Capacitance (C) and Resistance (R) of a material. LCR meter can help to measure dielectric properties including dielectric constant, dielectric loss, conductivity and tangential loss of a material. Using Wayne Kerr impedance analyzer, model Th 6500B dielectric measurements were performed within 100 to 5MHz frequency range These properties can be tested at various frequencies depending upon the frequency range of LCR meter. Fig. 3.7 is showing a LCR meter.

Fig. 3.7: LCR Meter Bridge

In the present work, for the measurement of dielectric properties, pellet of each sample was prepared using pellet die set and Hydraulic press. 1 gram mass of each product was taken. The size of pellets was 2 mm thick and 10 mm in diameter. A load of 4 tons for 2 minutes on each pellet was applied. Later on, annealing for 2 hours was done at 500 °C.

3.3.4 Vibrating Sample Magnetometer (VSM)

To measure the routine magnetic properties of magnetic materials like Ferrimagnetic, Ferromagnetic, Anti-ferromagnetic, Diamagnetic and Paramagnetic materials at varying temperatures, Simon Foner fabricated the first Vibrating sample Magnetometer (VSM) at Lincoln Laboratories in 1959.

Faraday's law of Induction is the basic principle of VSM. If a homogeneous magnetic field is applied on the sample and is vibrated at a small at fixed amplitude. The pick-up coils are stationary with respect to vibrating sample. The change in applied magnetic field generates voltage in stationary pick-up coils, coil 1 and coil 2 as shown in Fig. 3.8. With the help of this technique magnetic properties like saturation magnetization, remanence magnetization and coercivity of the sample can be measured by plotting a hysteresis curve [28].

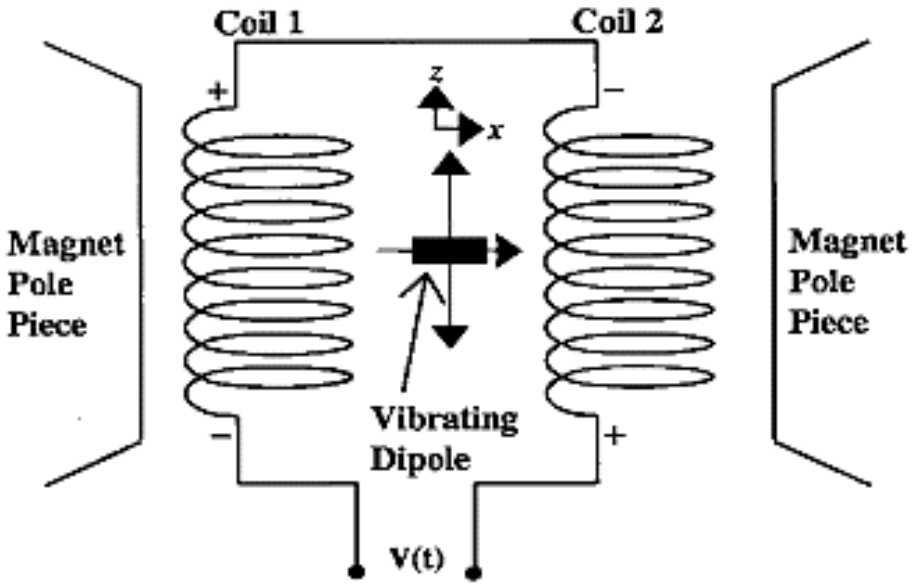

Fig. 3.8: Schematics VSM [28]

Chapter 4

Results and Discussion

4.1 XRD Analysis

The X-ray diffraction analysis on the pure and Co-doped Barium hexaferrite was conducted using a JEOL-JDX-9C X-ray diffractometer The major findings from the XRD analysis are discussed below:

4.1.1 XRD analysis of Barium Hexaferrite

The XRD Patterns of the pure and Co-doped Barium hexaferrite are shown in Fig. 4.1.

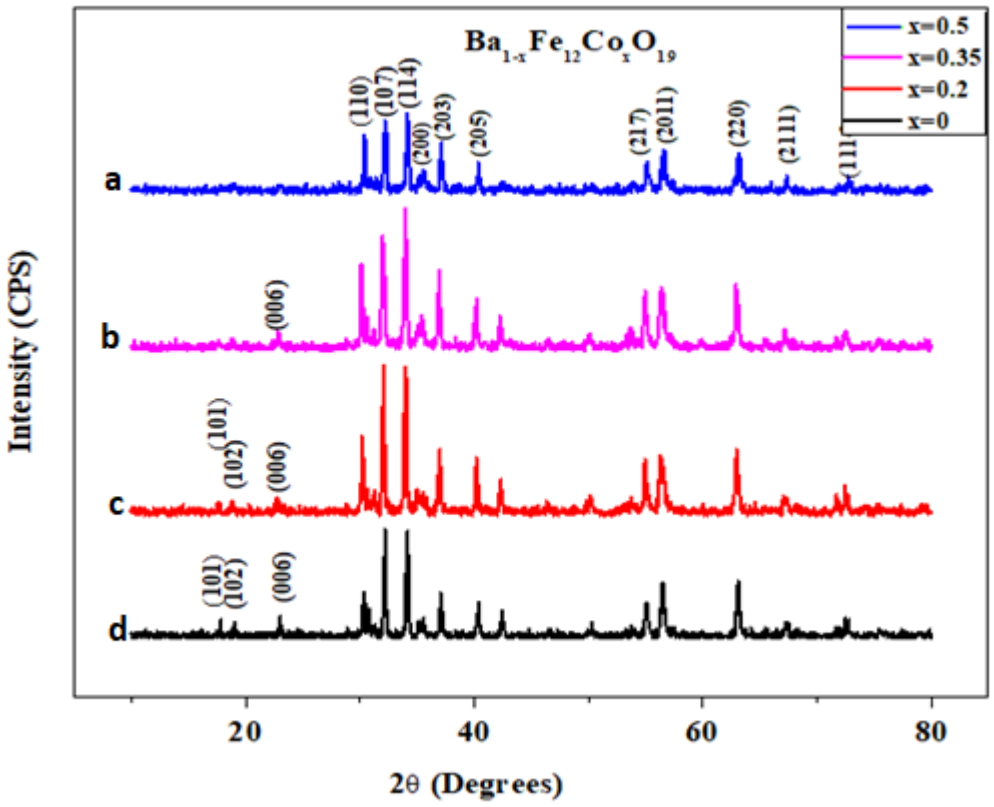

Fig. 4.1: XRD patterns of the pure and Co-doped Barium hexaferrite

The XRD pattern of the undoped sample at specific angle and d value matched with JCPDS data card No.27-1029 [24]. This matching confirmed the formation of the Barium hexaferrite sample with hexagonal structure. Fig. 4.1 also shows the well-separated strong diffraction peaks at planes (110), (107) and (114) for the pure sample.

The XRD patterns of the Co-doped Barium hexaferrite for x = 0.2,0.35, and 0.5 were matched with standard cards in terms of d Values to identify the phase. This matching showed that our values are in best agreement with JCPDS card 27-1029 showing the successful formation of Ba $Fe_{12}O_{19}$. Some peaks which were visible at (101), (102) and (006) planes for x = 0, disappeared with increase in the concentration of dopant up to x=0.5 (Fig. 4.1). For x = 0.35, the peaks at planes (101) and (102) were also absent. This showed a disturbance in the structure. Also, an important change was variation in intensity of strong lines as increased Co concentration up to x=0.5. The peak at the plane (107) was the strongest peak of pure sample (x = 0), but its intensity reduced at highest level of doping, x=0.5 as can be seen in pattern Fig 4.1a. Initially, in the pure sample peaks at plane (107) and (114) were in comparison. But with highest doping level intensity of (107) reduced as compared to peak at (114) plane as can be seen in pattern a (Fig. 4.1).

4.1.2 Crystallite Size Calculation

Using Debye Scherrer equation crystallite size was calculated for all prepared samples, which showed formation of nano particles within the range of 56 nm to 100 nm. Samples showed increasing trend in crystallite size as the concentration as dopant was increased. The detail of the calculated particle sizes for the various samples are summarized in Table 4.1.

Table 4.1 Lattice parameters, crystallite size of pure and doped Barium hexaferrite

Sr. No.	**Prepared Sample**	**Lattice parameters**		**Crystallite Size**
		a=b	c	
1	$Ba_{1-x}\ Fe_{12}O_{19}\ (Co)_x$ where x=0	5.895	23.09	56 nm
2	$Ba_{1-x}\ Fe_{12}O_{19}\ (Co)_x$ where x=0.2	5.895	23.09	67 nm
3	$Ba_{1-x}\ Fe_{12}O_{19}\ (Co)_x$ where x=0.35	5.895	23.09	67 nm
4	$Ba_{1-x}\ Fe_{12}O_{19}\ (Co)_x$ where x=0.5	5.893	23.05	100 nm

4.1.3 Lattice parameters calculation

Lattice parameter of all samples was calculated. A slight change in lattice parameters of sample doped at x=0.5 was observed as can be seen in Table 4.1. Remaining samples showed no change in lattice parameters. This is probably because of a minimal amount of dopant. This low content of dopant could not show any occupation parameters of Co at various sites in structure [17]. Miller indices and d values were in agreement with previously reported values [22].

4.2 SEM Analysis

An exemplary image obtained from the composition x=0 is shown in Fig. 4.2. The microstructure revealed that particles of samples were agglomerated and plated hexagonal shaped (Fig 4.2). This plate like hexagonal structure would be capable of reducing energy of EM waves by interfacial polarization [21]. This is reported that

pH of the particles can affect the morphology of particles using co-precipitation method. The morphology of particles is also based on reaction method and conditions such as calcination temperature and pH value [2]. This agglomeration has a reason of some kind of magnetic interactions between the particles [2]

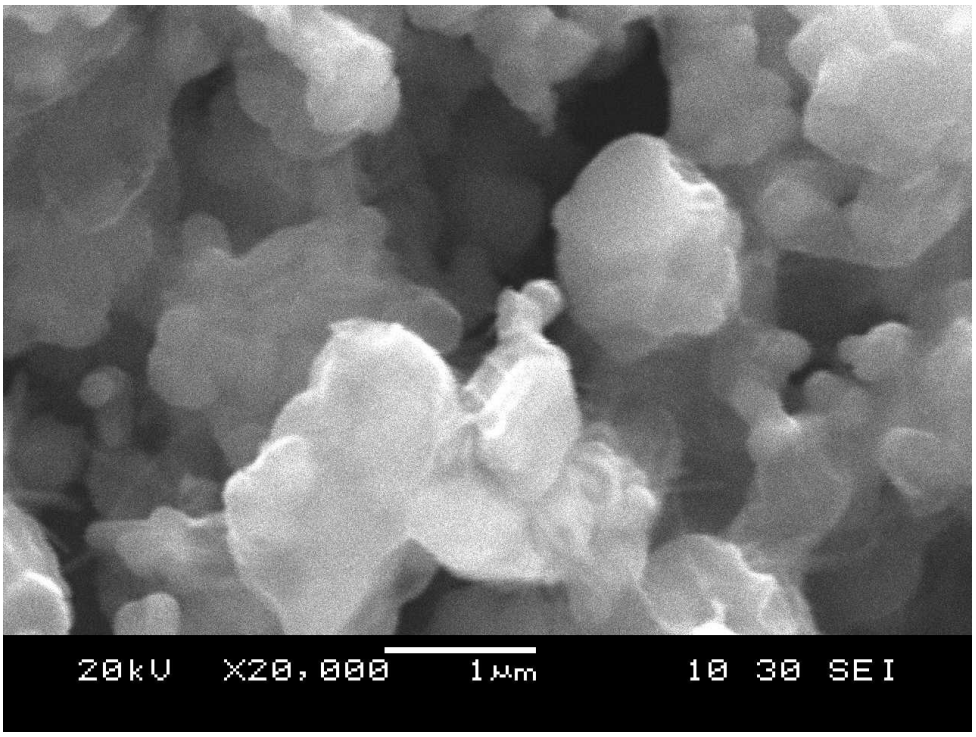

Fig. 4.2: SEM image of Barium hexaferrite

4.3 Dielectric studies

4.3.1 Dielectric Constant:

For dielectric constant, a decreasing trend with the increase of frequency for each prepared sample can be seen (Fig. 4.3). Eventually, this decreasing trend became constant at higher values of frequency between ln 10 to ln 15. This trend is attributed to the decrease in space charge polarization as the frequency rises. At higher frequencies beyond 550 Hz, the dipoles are unable to line up because of sudden shift of electric field applied [30]. At lower frequencies 300 to 550 Hz between ln 4 to ln 8 on Y axis, the value of dielectric constant is higher. The value of dielectric constant

for pure barium hexaferrite at 550 Hz is 1.66×10^2. Dielectric constant increased with increasing concentration of cation dopant $Ba_{1-x}Fe_{12}O_{19}(Co)_x$. The highest value of dielectric constant 5×10^3 at 550 Hz came for x=0.5. The increasing trend of dielectric constant with increasing concentration of dopant at x = 0.5 is shown in Fig. 4.4. The increase of dielectric constant values at lower frequencies can be well explained by Maxwell and Wagner model of space charge polarization [47]. According to this model, a dielectric material is divided into two parts, grains and grain boundaries. Grains are considered to be relatively conductive while grain boundaries are highly resistive. On application of electric field externally, the electrons started to move toward grain boundaries. Accumulation of electrons happens at the grain boundaries. Reason of this behavior is resistive nature of boundaries resulted in the polarization of material.

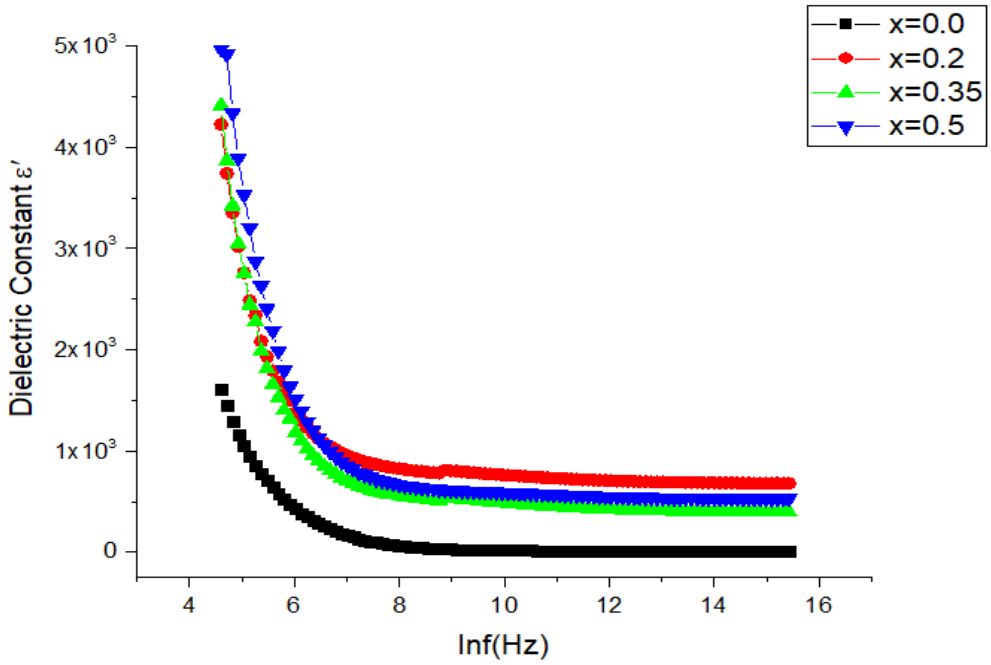

Fig. 4.3: Dielectric constant variation vs frequency for $[Ba_{1-x}Fe_{12}O_{19}(Co)_x]$

Accumulation of charge carriers occur at grain boundaries when the frequency of applied field is low, causing the space charge polarization resulting in dielectric constant of higher value. At higher frequencies between ln 10 to ln 15, a slow response is shown by these charge carries which result in decrease in space charge polarization and ultimately low values of dielectric constant (Fig. 4.3)

Increase in dielectric constant can be seen when metallic cation was added (Fig. 4.3). Metallic cations will reside in the tetrahedral sites, forcing the and Fe^{+3} ions to migrate toward the octahedral site. Hence the electron hoping of between different valence state of Fe on the octahedral site will increase resulting increased polarization. Also, the difference in electronegativity value of doped metallic cations and iron is less as compared to Barium, hence they will donate their electrons to iron resulting in increase of charge carrier. With increased number of charge-carriers the space charge polarization also increases so the dielectric constant will increase with high dopant concentration.

4.3.2 Dielectric Loss:

The trend of dielectric loss with frequency is shown in Fig. 4.4. The values of dielectric loss are decreasing with increase of frequency beyond 550 Hz between ln 7 to ln 15. With the increasing concentration of dopant, increase in dielectric loss value of the material can be seen. At lower values between ln 6 to ln 8 of frequency, dielectric loss has higher values. Dielectric loss values start to decrease as the frequency of the applied field is increased.

The decreasing behavior of dielectric loss at higher frequencies can be explained by Koop's theory. According to this theory, polarization requires more energy in low frequency regions because of highly resistive grain boundaries. Hence energy losses are high. Whereas resistivity of grain boundaries in high frequency region is relatively lower so the polarization of material become slight easy. Hence the dielectric losses start to decrease [48]. With increase in dopant concentration, increase in dielectric loss can be seen in the Fig. 4.4. Movements of charge carriers in the alternating electric field cause the dissipation of energy and hence the dielectric loss occurs. As the doping concentration is increased, number of charge carrier moving in the alternating electric field also increase causing high dielectric losses. Therefore, dielectric loss for sample doped at x = 0.5 concentration has the highest value of dielectric loss at ln 6 value, shown by arrow (Fig. 4.4).

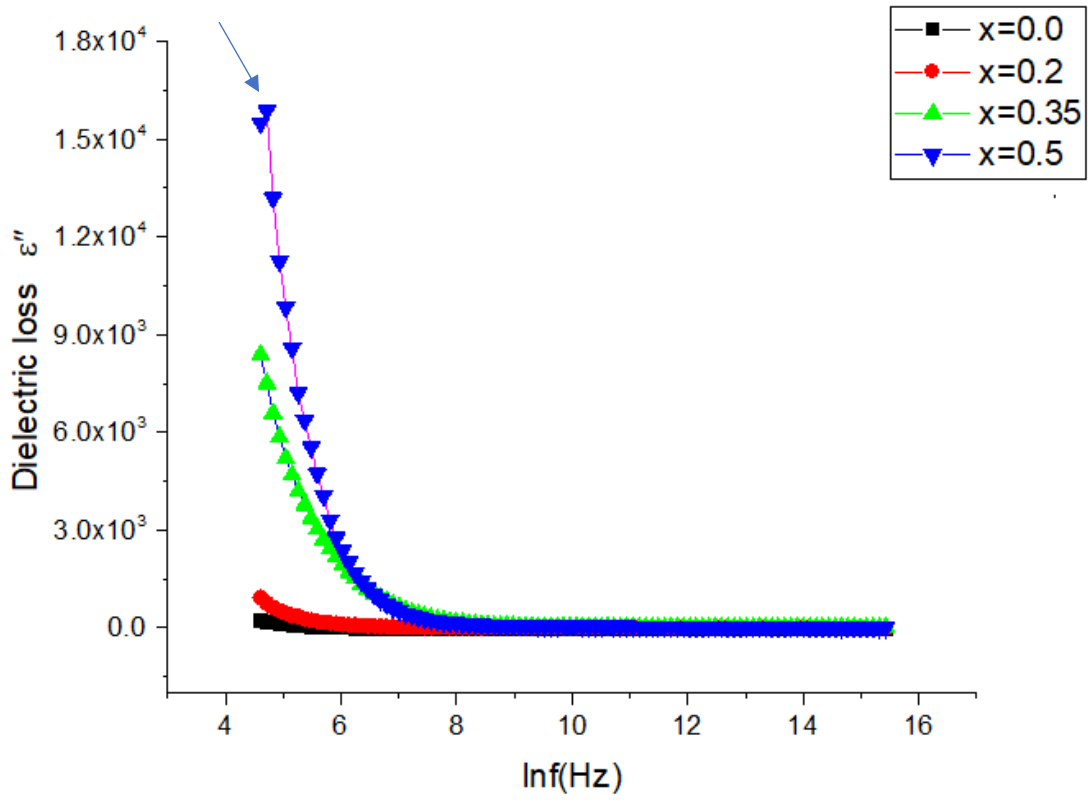

Figure 4.4: Dielectric loss variation vs frequency for [$Ba_{1-x}Fe_{12}O_{19}(Co)_x$]

4.3.3 Dielectric Tangent Loss

The dielectric tangential loss is also showing increasing trend with increased level of doping. It has higher values at low frequencies up to 550 Hz between ln 4 to ln 9 (Fig. 4.5). This is due to the reason that hopping of electron between Fe^{+3} and Fe^{+2} is higher at low frequency of ln 4 to ln 9. whereas this hopping reduces at higher frequency between ln 9 to ln 15, resulting in decrease of dielectric tangent loss values.

The value of tangent loss for pure Barium hexaferrite is 2.25 whereas when Barium hexaferrite is doped with x=0.5 Co, the tangent loss value is increased to 4.5. This increase in dielectric tangent loss with concentration can be attributed to increase number of charge carriers in doped samples which require high amount of applied field energy for space charge polarization. Hence the dielectric tangent loss increased [30].

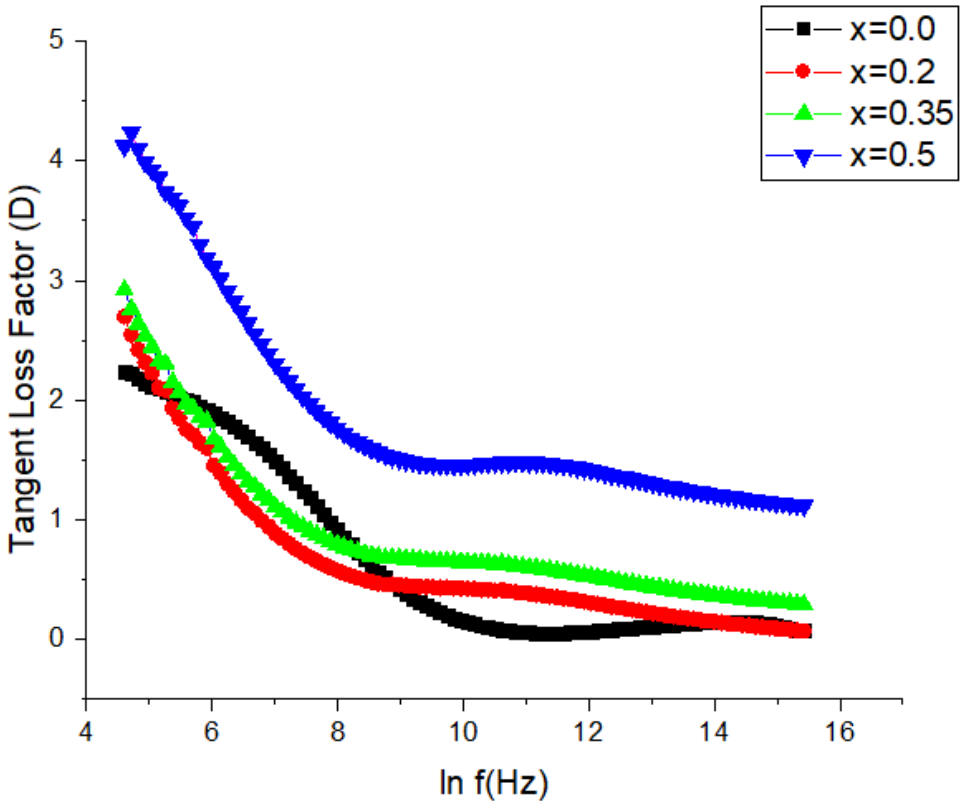

Fig. 4.5: Tangential loss variation vs frequency for [$Ba_{1-x}Fe_{12}O_{19}(Co)_x$]

4.3.4 AC Conductivity

At low frequency range of 550 Hz between ln 4 to ln 10, the ac conductivity is independent of the frequency and an increasing trend can be seen with increase in frequency within range of 1 MHz with ln value of 10 to ln value 14 (Fig. 4.6). This behavior is in accordance to Maxwell-Wagner type [47]. According to this, at lower frequency between ln 4.5 to ln 10 conductivity values are low due to large hindrance at grain boundaries (related to dc conductivity) for the movement of electrons. As the frequency increases, the conductivity across the grain boundaries increases due to the more effective hopping of electrons between Fe^{2+} and Fe^{3+} ions. Major contribution is from grain boundaries because of the difference between radii of Co and Ba.

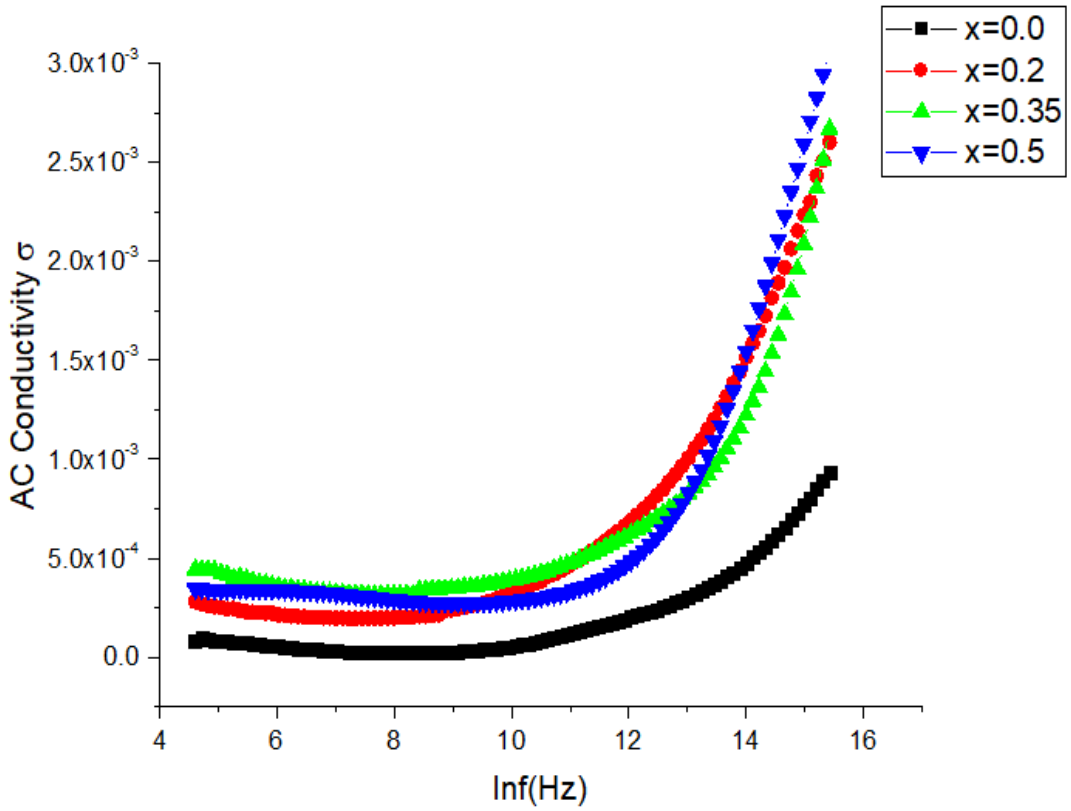

Fig. 4.6: Conductivity variation vs frequency for [$Ba_{1-x}Fe_{12}O_{19}(Co)_x$]

Conductivity in ferrites can also be described with Verwey mechanism which described that conductivity in ferrites is based upon hopping of electrons between ions in different valence states of similar specie (Element) [32].

4.3.5 Electric Modulus

To explains the relaxation and conduction behavior of materials electric modulus plots are useful. Fig. 4.7 shows the frequency dependent real and imaginary part of electric modulus at constant temperature with different compositions of Cobalt. At lower frequencies up to 500 Hz, M′ values are very small which represents negligible electrode effect. At higher frequencies within MHz range increase in the value of M′. The reason of this increase is the short-range mobility of charge carriers [49]. Two different peaks at low and high range frequencies represent that resistance of grains and grain boundaries is playing their roles in the conduction mechanism of the system [50].

In figure 4.8 M″ two clear peaks shown with the help of arrow representing the grain and grain boundaries effect. This plot also represents a clear change in position of relaxation peaks to frequencies between ln 12 to ln 15 from lower frequency range between ln 4.5 to ln 10 at 550 Hz. The increase of Cobalt content is responsible for this. In low frequency region charge carriers moving over long distances and ascribed to hopping process. And in high frequency region between ln 12 to ln 15 charge carriers are moving over a small distance due to relaxation polarization.

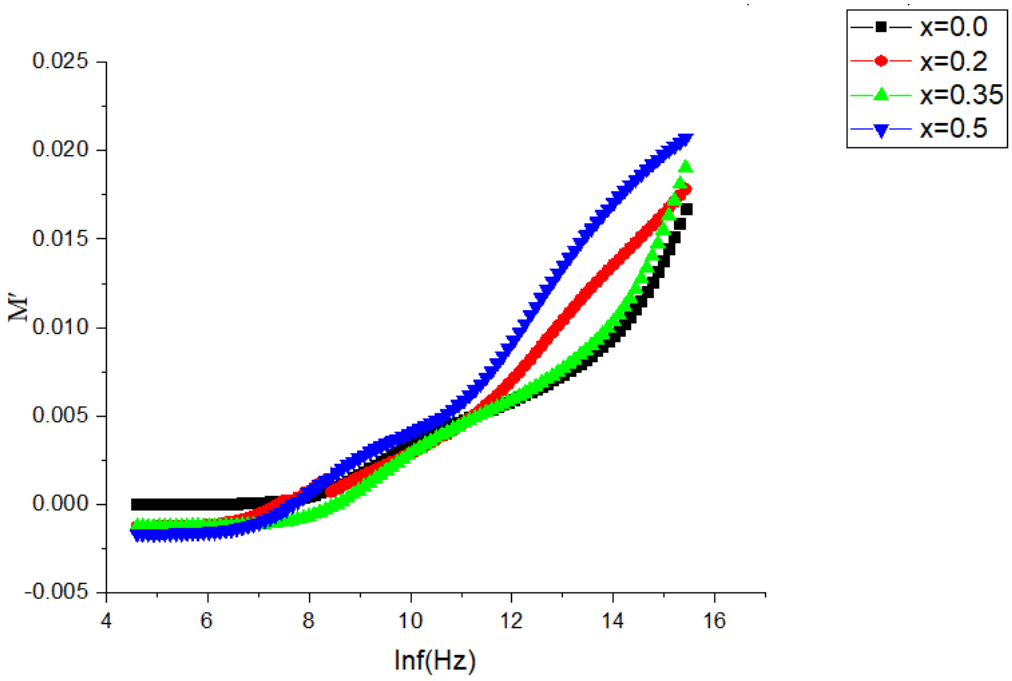

Fig. 4.7: Dielectric modulus variation vs frequency for [$Ba_{1-x}Fe_{12}O_{19}(Co)_x$]

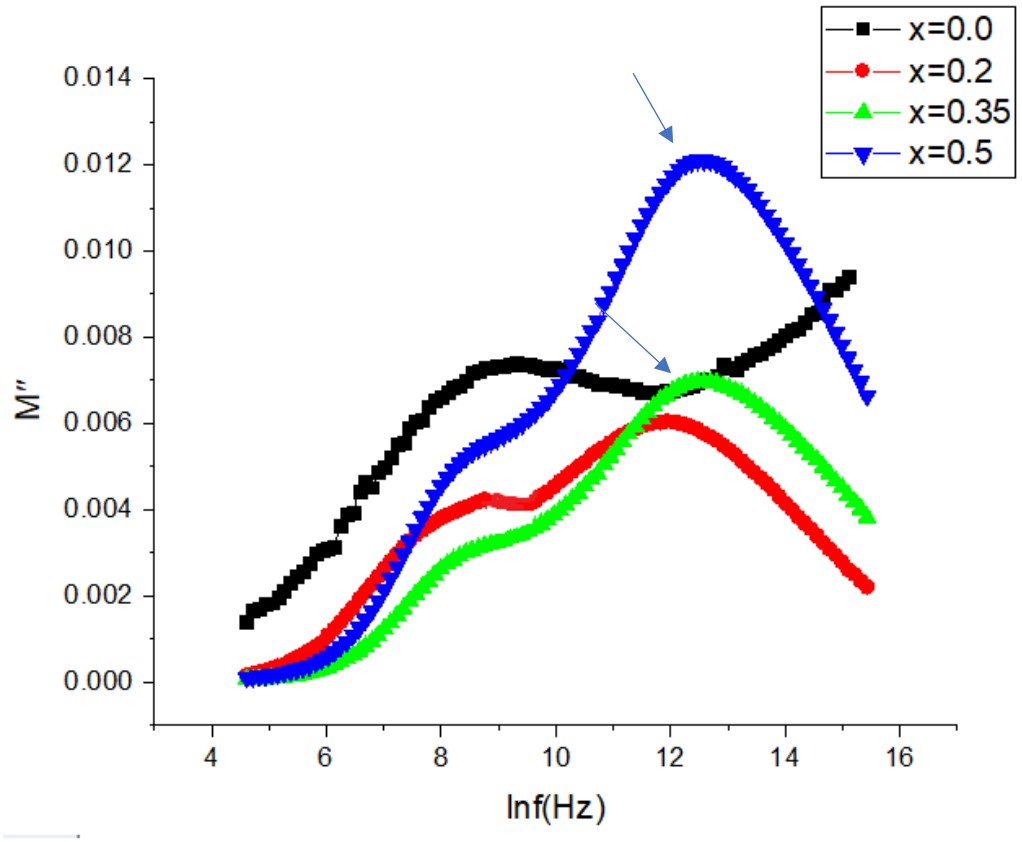

Fig. 4.8: Complex value of modulus vs frequency [$Ba_{1-x}Fe_{12}O_{19}(Co)_x$

4.3.6 Cole Cole Plot

To understand frequency dependent charge carrier transport system in materials as a function of microscopic parameters like time of charge relaxation dispersion and its variation, ions carriers hopping rate and space charge polarization, depending on compositional variation, complex electric modulus spectroscopy can be used. In Fig. 4.9, below semi circles are showing capacitive grain contribution effect and on the other end semi-circle which is present at high frequency value shown with the help of arrows, reveals capacitive grain boundary effect.

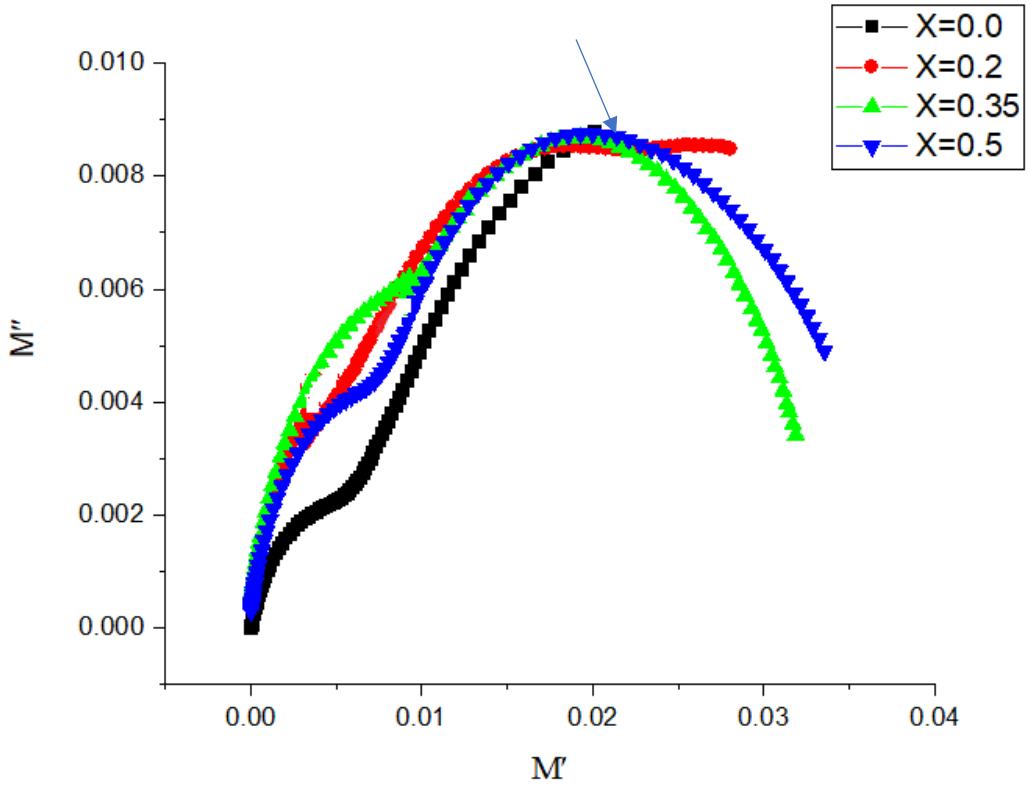

Fig. 4.9: Cole Cole plot [$Ba_{1-x}Fe_{12}O_{19}(Co)x$]

Reason may be dissimilarity between ionic radii of Co and Barium. So, number of grain boundaries has increased and plying their role and showing their contribution. Surface charge polarization is responsible for these effects which is explained by Maxwells Wagner theory [47].

Table 4.2 given below is presenting a complete summary of behavior of dielectric constant, dielectric loss, tangential loss and AC conductivity of pure and doped samples. Increasing trend of all the dielectric properties as the doping level has increased can be seen. In short dielectric constant has increased 3 times, increase in dielectric loss is 71 times, Tangential loss and conductivity has increased 2 and 3 times, respectively.

Table 4.2 Summary of dielectric properties of pure and Co doped Barium hexaferrite.

Dielectric Property	**Ba $Fe_{12}O_{19}$**	**Ba_{1-x} $Fe_{12}O_{19}$ $(Co)_x$ at x=0.2**	**Ba_{1-x} $Fe_{12}O_{19}$ $(Co)_x$ at x=0.35**	**Ba_{1-x} $Fe_{12}O_{19}$ $(Co)_x$ at x=0.5**
Dielectric Constant ε′	1.66×10^3	4.28×10^3	4.48×10^3	5.0×10^3
Dielectric Loss ε″	2.24×10^2	1.1×10^3	8.5×10^3	1.6×10^4
Tangential Loss D	2.25	2.75	3.0	4.3
AC Conductivity σ S/m	9.6×10^{-4}	2.6×10^{-3}	2.7×10^{-3}	3×10^{-3}

4.4 Magnetic Measurements

Using VSM, saturation magnetization M_s, remanence magnetization M_r and coercive force H_c of pure and doped sample (x = 0.0, x= 0.5) were measured. The Hysteresis curve of both samples is shown in Fig. 4.10.

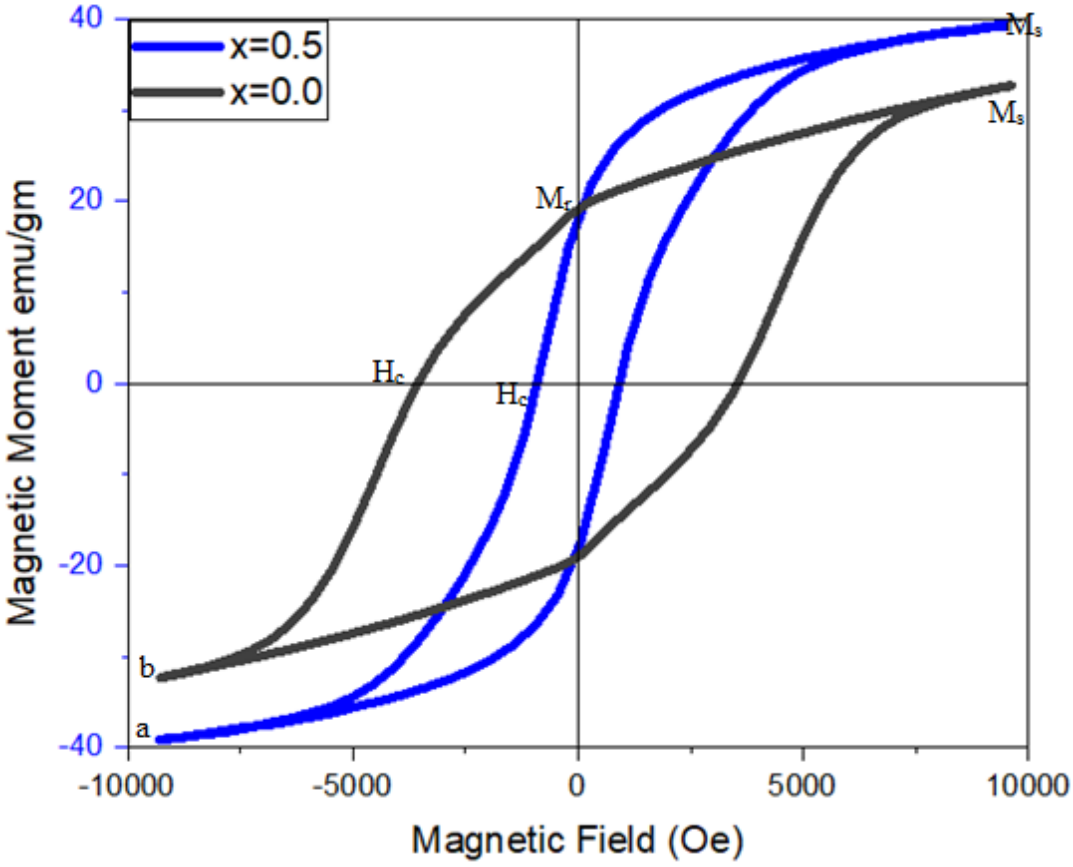

Fig. 4.10: Hysteresis Curve of X=0.0, X=0.5 [$Ba_{1-x}Fe_{12}O_{19}(Co)_x$]

The magnetic hysteresis loop of pure sample (x = 0) is showing that it has large area of hysteresis curve. This large area proves that undoped sample is a hard magnetic material due to high coercivity value of 3567 Oe. The curve obtained from Co doped sample at x = 0.5 (curve a) has smaller area as compared to undoped sample. Therefore, doped sample has smaller value of coercivity i.e., 918 Oe proving it soft magnetic material in nature (Fig. 4.10). Pure Barium hexaferrite has high value of coercivity Hc because it possesses uniaxial anisotropy i.e., it has one easy axis along the c-axis [17]. Whereas the magnetic properties of doped hexaferrites strongly based on electronic configuration of doped cation and their trend to occupy various Fe sites in magneto plumbite structure of hexaferrites [51]. Doping of Co was done at $4f_2$ site,

which is major contributor to magneto crystalline anisotropic, has negative impact on this magneto crystalline anisotropy so coercivity decreased. It is also clear that undoped sample has higher value of saturation magnetization (Fig 4.10). A slight increase up to 39 emu/gm from 32 emu/gm in saturation magnetization of doped sample is observed which may be due to same magnetic nature of Iron and Cobalt [17]. Remanence magnetization (M_r) value of pure sample is 18 emu/gm whereas for doped sample at x = 0.5 it is 17 emu/gm. The decrease in coercivity value and slight change in saturation magnetization values of doped hexaferrite prepared for EMI shielding application has already been reported by other researchers. Susilawati et al. in a recent work has reported same trend of decrease in coercivity and saturation magnetization of the Mn doped Barium hexaferrite [23].

Table 4.3 has a summary of magnetic properties of pure and doped Barium hexaferrite at x=0.5. This table clarifies the magnetic behavior of material based upon increase in doping concentration.

Table 4.3 Summary of magnetic properties of pure and doped Barium hexaferrite at x=0.0 and x=0.5

Magnetic Property	**$Ba_{1-x}Fe_{12}O_{19}(Co)_x$ at x=0.0**	**$Ba_{1-x}Fe_{12}O_{19}(Co)_x$ at x=0.5**
Saturation Magnetization M_s	32 emu/gm	39 emu/gm
Remanence Magnetization M_r	17 emu/gm	18 emu/gm
Coercivity H_c	3567 Oe	918 Oe

Summary

In the current study, the Co-doped Barium hexaferrite with different cobalt concentrations of x = 0, 0.2, 0.35 and 0.5 were prepared by using a chemical co-precipitation method. The formation of $Ba_{1-x}Fe_{12}(Co)_x O_{19}$ at x=0.0, 0.2, 0.35, 0.5 was confirmed using X-ray diffraction analysis. The hexagonal crystal structure of synthesized Barium hexaferrite was confirmed when d- values obtained from XRD were matched with standard JCPDS cards, using match software. Debye Scherrer's formula was to calculate the crystallite size, which was found to be 56 nm to 100 nm. The morphology of the preprepared pure Barium hexaferrite powder was studied via SEM, which revealed that the particles were in agglomeration form.

Dielectric properties were studied at room temperature using an impedance analyzer. The dielectric constant, dielectric loss and conductivity showed increasing trend with increase in Co content.

A vibrating sample magnetometer (VSM) was used to measure the magnetic properties i.e., saturation magnetization and coercivity of the prepared samples. At x = 0.5 magnetic coercivity value was decreased to 918 Oe from 3567 Oe, which is better than the already reported values [24]. The results of magnetodielectric studies suggest that the Cobalt doped Barium hexaferrite can be a good candidate for Electromagnetic Interference Shielding within the GHz range.

References

[1] M. Kaur, S. Kakar, D. Mandal, in: ICECT3rd Int. Conf. Electron. Comput. Technol., 33 (2011) 1–5.

[2] R.S. Alam, M. Moradi, M. Rostami, H. Nikmanesh, R. Moayedi, Y. Bai, J. Magn. Magn. Mater. 381 (2015) 1–9.

[3] John, H., et al., Conducting polyaniline composites as microwave absorbers. Polymer composites, 28(5) (2007) 588-592.

[4] K.S. Martirosyan, E. Galstyan, S.M. Hossain, Y.J. Wang, D. Litvinov, Mater. Sci. Eng. B Solid-State Mater. Adv. Technol. 176 (2011) 8–13.

[5] R. Wilson, G. George, K. Joseph, in: Mater. Potential EMI Shield. Elsevier, 5 (2020) 1–8.

[6] K. Sreedeviamma Dijith, Remadevi Aiswarya, Mathew Praveen, Saju Pillai, K. Peethambharan Surendran, Mater. Chem. Front. 2 (2018) 1829–1841.

[7] K. Ji, H. Zhao, J. Zhang, J. Chen, Z. Dai, Appl. Surf. Sci. 311 (2014) 351–356.

[8] M. Rahaman, T.K. Chaki, D. Khastgir, Polym. Compos. 32 (2011) 1790–1805.

[9] R. Singh, S.G. Kulkarni, Polym. Bull. Mat Sci. 71 (2014) 497–513.

[10] S. Iqbal, S. Ahmad, in: Mater. Potential EMI Shield. Elsevier, 55 (2020) 257–266.

[11] S. Iqbal, S. Ahmad, in: Mater. Potential EMI Shield. Elsevier, 23 (2020) 257–268.

[12] V. Pratap, A.K. Soni, S. Dayal, S.M. Abbas, A.M. Siddiqui, N.E. Prasad, J. Magn. Magn. Mater. 465 (2018) 540–545.

[13] W. Li, X. Qiao, M. Li, T. Liu, H.X. Peng, Mater. Res. Bull. 48 (2013) 4449

[14] J. Liu, J. Zhang, Y. Li, M. Zhang, Mater. Chem. Phys. 163 (2015) 470–477.

[15] G. Gultom, M. Rianna, P. Sebayang, M.G.-C.S. in Thermal, 168 (2020) 320

[16] C. Dong, X. Wang, P. Zhou, T. Liu, J. Xie, L. Deng, J. Magn. Magn. Mater. 354 (2014) 340–344.

[17] D.A. Vinnik, A.Y. Tarasova, D.A. Zherebtsov, L.S. Mashkovtseva, S.A. Gudkova, S. Nemrava, A.K. Yakushechkina, A.S. Semisalova, L.I. Isaenko, R. Niewa, Ceram. Int. 41 (2015) 9172–9176.

[18] S. Iqbal, G. Kotnala, J. Shah, S. Ahmad, Mater. Res. Express 6 (2019) 320-350

[19] W. Widanarto, F.M. Rahayu, S.K. Ghoshal, M. Effendi, W.T. Cahyanto, Results Phys. 5 (2015) 253–256.

[20] S.P. Gairola, V. Verma, L. Kumar, M.A. Dar, S. Annapoorni, R.K. Kotnala, Synth. Met. 160 (2010) 2315–2318.

[21] S. Goel, A. Garg, R.K. Gupta, A. Dubey, N.E. Prasad, S. Tyagi, Mater. Res. Express 7 (2020) 220-235

[22] P. Shepherd, K.K. Mallick, R.J. Green, J. Mater. Sci. Mater. Electron. 18 (2007) 527–534.

[23] Susilawati, A. Doyan, Khalilurrahman, in: AIP Conf. Proc., American Institute of Physics Inc. 58 (2017) 040007.

[24] K.K. Mallick, P. Shepherd, R.J. Green, J. Magn. Magn. Mater. 312 (2007) 418

[25] K.K. Mallick, P. Shepherd, R.J. Green, J. Eur. Ceram. Soc. 27 (2007) 2045

[26] N. Yasmin, M. Mirza, S. Muhammad, M. Zahid, M. Ahmad, M.S. Awan, A. Muhammad, J. Magn. Magn. Mater. 446 (2018) 276–281.

[27] M.S. Vijaya, G. (Gopala) Rangarajan, Mat Science 1 (2004) 590.

[28] B. Cullity, C. Graham, 7 (2011) 380-397.

[29] V. Iacovacci, G. Lucarini, L. Ricotti, A. Menciassi, in: Lab-on-a-Chip Fabr. Appl., InTech, 1 (2016) 218-290

[30] M.A. Rafiq, M. Waqar, Q.K. Muhammad, M. Waleed, M. Saleem, M.S. Anwar, J. Mater. Sci. Mater. Electron. 29 (2018) 5134–5142.

[31] N. Kumari, V. Kumar, S.S.-R. Advances, Pubs.Rsc.Org 33 (2015), 226-250.

[32] Levin, M. and M. Miller, Maxwell's" Treatise on Electricity and Magnetism". Soviet Physics Uspekhi, **24**(11) (1981) 904.

[33] A. Lloyd, Key Eng. Mater.124 (1996) 175–184.

[34] V.N. Dhage, M.L. Mane, M.K. Babrekar, C.M. Kale, K.M. Jadhav, J. Alloys Compd. 509 (2011) 4394–4398.

[35] E. ALBERS-SCHOENBERG, J. Am. Ceram. Soc. 41 (1958) 484–489.

[36] T.F.W. Barth, E. Posnjak, Zeitschrift Für Krist. - Cryst. Mater. 82 (2014) 325

[37] D.S. Mathew, R.S. Juang, Chem. Eng. J. 129 (2007) 51–65.

[38] V.F. Kitaeva, E. V. Zharikov, I.L. Chistyi, Phys. Status Solidi 92 (1985) 475–488.

[39] P. Coutinho, F. Cunha, P.B.-S.S. Communications, 82 (2017) 325–341.

[40] H. Kojima, Handb. Ferromagn. Mater. 3 (1982) 305–391.

[41] S.F. Shaikh, M. Ubaidullah, R.S. Mane, A.M. Al-Enizi, Spinel Ferrite Nanostructures for Energy Storage Devices 55 (2020) 51–82.

[42] Kaiser, M., Electrical conductivity and complex electric modulus of titanium doped nickel–zinc ferrites. Physica B: Condensed Matter, 407(4) (2012) 606-613.

[43] M. Radwan, M.M. Rashad, M.M. Hessien, J. Mater. Process. Technol. 181 (2007) 106–109.

[44] J. Epp, Mater. Charact. Using Nondestruct. Eval. Methods 55 (2016) 81–124.

[45] M. Kurian, S. Thankachan, D.S. Nair, A. E. K, A. Babu, A. Thomas, B. Krishna K. T, J. Adv. Ceram. 4 (2015) 199–205.

[46] K.C.A. Smith, C.W. Oatley, Br. J. Appl. Phys. 6 (1955) 391.

[47] M.L. Levin, M.A. Miller, Sov. Phys. Uspekhi 24 (1981) 904.

[48] J. Sharma, N. Sharma, J. Parashar, V.K. Saxena, D. Bhatnagar, K.B. Sharma, J. Alloys Compd. C (2015) 362–367.

[49] M. Kaiser, Phys. B Condens. Matter 407 (2012) 606–613.

[50] P. Behera, S. Ravi, Solid State Sci. 89 (2019) 139–149.

[51] J. Slama, A. Gruskova, M. Papanova, D. Kevicka, R. Dosoudil, V. Jancarik, A. González, G. Mendoza, J. Magn. Magn. Mater. 27 (2004) 385–387.